RICE UNIVERSITY

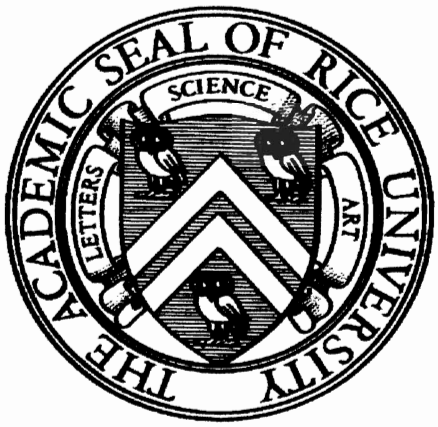

Interaction of Xenon Rydberg Atoms with Conductive Surfaces: The Effects of Stray Fields

by

Dennis Neufeld

Doctor of Philosophy

Houston, Texas

July, 2010

RICE UNIVERSITY

Interaction of Xenon Rydberg Atoms with Conductive Surfaces: The Effects of Stray Fields

by

Dennis Neufeld

A Thesis Submitted
in Partial Fulfillment of the
Requirements for the Degree

Doctor of Philosophy

Approved, Thesis Committee:

F.B. Dunning, Chair
Sam and Helen Worden
Professor of Physics

P. Noordlander
Professor of Physics
Professor of ECE

P. Brooks
Professor of Chemistry

Houston, Texas

July, 2010

Interaction of Xenon Rydberg Atoms with Conductive Surfaces: The Effects of Stray Fields

Dennis Neufeld

Abstract

The ionization of xenon Rydberg atoms at metallic surfaces is examined. The data show that, when the effects of stray electric "patch" fields present on the surface are taken into account, ionization is well described by a simple over-the-barrier model. The patch fields are determined from direct measurements of the potential variations across the target surfaces using Kelvin probe force microscopy. Monte Carlo techniques are used to model the atom-surface interaction. The results confirm the important role that patch fields can play during Rydberg atom-surface interactions and suggest that such interactions can provide a sensitive probe of stray fields at surfaces.

To demonstrate this, measurements of the threshold conditions required to observe ions resulting from surface ionization are used to estimate how large such stray fields can be. The data show that the stray fields can be sizable, as large as $\sim 10^3\ V \cdot cm^{-1}$ 100 nm from the surface and $\sim 10\ V \cdot cm^{-1}$ 500 nm from the surface, and illustrate the potential of Rydberg atoms for detecting and characterizing surface electric fields.

Methods to enhance the surface ionization signal using electrode arrays patterned on a surface are investigated. Simulations show that bias voltages applied to a series of parallel wires comprised of two interleaved comb-shaped electrodes can have a dramatic impact on ion collection efficiency. It is suggested that such a surface can be used to efficiently collect low-n Rydberg atoms ($n \gtrsim 10$). Significant progress towards fabrication of a functioning surface of 1 μm wide wires with 1 μm spacing is documented.

Acknowledgments

There are many people who deserve my thanks for making this accomplishment possible. Most importantly I have to thank my wife, Amber. She has put up with the humidity, traffic, horrible air quality and mosquitoes for far too long. I know it has been extremely difficult for such a family-oriented person not to have a single relative within a 2-state radius. She has made a tremendous personal sacrifice for my education, and for that I am truly grateful.

I also have to thank many of my fellow graduate students. Zach Keane was a crucial resource for my nano-fabiation endeavors. His advice on materials, processes, and techniques was invaluable. Even the lab at UT Austin was his suggestion. I must although thank my junior student, Yu Pu. His contributions towards computing field strengths from Fourier components were brilliant, and fundamental to the evolution of the model.

I also owe my gratitude to the many other graduate and post-doctoral students who have assited me at one point or another during my study at Rice. These include Leonard Suess, Yi Liu, Fred Kontur, Jim Lancaster, Habib Aliabadi, Hardin Dunham, Wei Zhao, Changhao Wang, and Shuzhen Ye. In particular I have to thank Jeff Mestayer, Brendan Wyker, and Matt Cannon for their friendship, and for making life

as a grad student a little bit easier.

I have to thank my family for their love and support. The values my parents taught me and the examples they set have helped shape me into who I am today, and have motivated me to strive for this accomplishment.

Lastly, I wish to express my gratitude to the Robert A. Welch foundation and the National Science Foundation for their generous support.

Contents

Tables

Figures

Chapter 1

Introduction

The present experiments are designed to probe the interaction between a Rydberg atom and a nearby surface. Rydberg atoms are atoms with a single valence electron excited to state of large principal quantum number n. Due to their large physical size and weak binding, Rydberg atoms are particularly sensitive to external electric fields and hence are easily perturbed by the presence of surface.

As Rydberg atoms approach a surface, image charge interactions modify the potential which binds the Rydberg electron to its ionic core, forming a potential barrier. At some critical distance from the surface, the height of the potential barrier dips below the energy of the excited electron allowing it to "tunnel" into a vacant resonant energy level in the surface. The resulting core ion is attracted to the surface by its image charge field where it is lost through Auger neutralization. This loss can be prevented by application of an ion collection field perpendicular to the surface. Since the strength of the image charge field, and hence the DC field required to counteract it, depends critically on the distance at which ionization occurs, measurement of the fraction of atoms collected at a given applied field can, in principle, yield some information about the atom-surface separation at which ionization occurs, i.e. the ionization distance. Recent experiments have demonstrated that local stray electric

fields present at surfaces (or "patch" fields) modify the potential barrier and can have a dramatic impact on the distance at which ionization occurs [1–3].

This thesis will discuss the ionization of xenon nf Rydberg atoms with values of n ranging from n=14 to n=50, near several surfaces. The work presents a detailed study of the effects of stray surface electric (or "patch") fields on the ionization mechanisms operative and the ionization distances. This work also examines the utility of Rydberg atoms as a probe of stray electric (or "patch") fields present on a surface. Understanding of such stray fields is of fundamental importance for studies of short-range surface phenomena such as the Casimir-Polder force [4] and non-contact friction [5,6], or when trapping atoms or ions near a surface [7,8].

1.1 Rydberg Atoms

1.1.1 Introduction to Rydberg Atoms

A Rydberg atom is characterized by a high principal quantum number n, i.e., one (or more) of its electrons is in a highly-excited state. The excited electron is bound by Coulomb attraction to the ionic core and the energies of the bound levels (for hydrogen) follow the usual Rydberg series [9]

$$E_n = -\frac{R}{n^2} \tag{1.1}$$

where R is a universal constant known as the Rydberg constant and has the value $R = 1.0973732 \times 10^{-5}\ cm^{-1} = 13.607\ eV$. For non-hydrogenic atoms a correction needs to be made to Eq. 1.1 arising from the fact that the inner electrons do not

entirely screen the nuclear charge from the excited electron. This is particularly true for multi-electron atoms in low angular momentum states where there is significant overlap between the wavefunctions of the ion core and Rydberg electron. In a more semi-classical description, there is a high probability of finding the electron near the nucleus where it can polarize or even penetrate inner electron cloud near the ion core. This results in a deviation from the pure Coulombic $1/r$ potential at small r, modifying the energy levels. This leads to tighter binding and is taken into account through the quantum defect, effectively a reduction of the principal quantum number. With the inclusion of the quantum defect, δ, Eq. 1.1 becomes

$$E_n = -\frac{R}{(n-\delta)^2} \tag{1.2}$$

Knowledge of the quantum defect becomes especially important when modeling the Rydberg atom or when calculating the photon energies, i.e. the laser wavelengths required for excitation to particular Rydberg states.

1.1.2 Physical Properties

Rydberg atoms with large values of principle quantum number, n, possess physical properties that are greatly exaggerated when compared to those of low-lying or ground state atoms [9]. A few of these properties are listed in Table 1.1 along with their n dependence and typical numerical values for a few specific values of n. One property of particular importance to this work is the classical field ionization threshold (section 2.1.2), which scales as $1/n^4$. Because the field ionization threshold is

Property	Scaling	$n = 1$	$n = 10$	$n = 100$
Mean Radius	n^2	0.53 Å	5.3 nm	0.53 μm
Binding Energy	$\frac{1}{2n^2}$	13.6 eV	136 meV	13.6 μeV
Orbital Period	$2\pi n^3$	0.15 fs	0.15 ps	0.15 ns
Energy Spacing	$\frac{1}{n^3}$	10.2 eV	10.2 meV	10.2 μeV
Radiative Lifetime	$\tau_0(E) \cdot n^3$	500 ps	500 ns	500 μs
Classical Field Ionization Threshold	$\frac{1}{16n^4}$	3×10^8 V/cm	33 kV/cm	3.3 V/cm

Table 1.1 : Scaling (in atomic units) of various physical properties of (hydrogenic) Rydberg atoms with respect to n. Included are numerical values at selected principal quantum numbers n. The radiative lifetimes given are for zero-field, with $\tau_0(0) \sim 500ps$

extremely sensitive to n, the range of n-levels employed in this work (n=14 to n=50) spans almost two orders of magnitude in critical field for ionization. Since it is expected that magnitude of stray electric fields will reduce with increasing distance from the surface, the n-level becomes a critical parameter allowing for the investigation of ionization mechanisms over a wide range of atom-surface separations.

1.2 Rydberg Atoms on Surfaces

1.2.1 History

Several attempts have been made to understand the resonant surface ionization process. The first experiment along these lines was performed by Kupriyanov [10] who investigated the transmission of excited atoms through a metal grid. He simply noted that highly excited atoms were ionized when in the proximity of a metal surface. Later Fabré *et al* [11] performed a similar experiment passing a beam of Na(nd) Rydberg atoms through an array of slits in the hope of relating the size of the Rydberg atom to that of the slit. A hard sphere model suggested that destruction of Rydberg atoms occurs when they approach within a distance of $4.5 \cdot n^2$ a.u. from a surface, which is much greater than calculations predicted using an image charge model. This discrepancy was attributed to local electric fields produced by impurities on the surface of the slits.

McCown *et al* [12] later confirmed Fabré's conclusion that contamination can enhance Rydberg atom destruction. By measuring the transmission of lithium Rydberg atoms through a gold mesh as a function of time, the effects of contamination of the mesh as lithium was deposited and subsequently absorbed water were monitored. Model calculations confirmed the importance of local fields and supported the idea that the atomic size was less than suggested by Fabré.

At the same time McCown was confirming Fabré's results, Gray *et al* [13] set out to investigate the ion production from K(nd) Rydberg atoms incident at grazing in-

cidence on a gold surface. The atoms were incident at 2° and the surface was heated to 80°C in an attempt to prevent potassium atoms from sticking to the surface and contaminating it. An electric field was applied perpendicular to the surface to pull the resulting ions towards a position sensitive detector. Despite the precautions taken to keep the surface clean, contamination from potassium deposition prevented meaningful conclusions being drawn from the data. As the surface became contaminated with potassium, which subsequently absorbed water, strong spurious local fields were generated at the surface which resulted in enhanced ion collection.

From the early observations of excited atoms ionizing near metal surfaces to attempts to measure the atom-surface separation at which ionization occurs, issues associated with surface contamination have been a major limiting factor. Here we attempt to overcome this limitation using xenon Rydberg atoms. Advances in laser and vacuum technology allow the excitation of xenon metastable atoms to Rydberg states under ultra-high vacuum (UHV) conditions. The low pressures in the interaction region coupled with the inert properties of xenon allow surface studies to be conducted under stable and potentially well-defined surface conditions.

1.2.2 Current Approach

The goal of the current experiment is to determine the atom-surface separation at which ionization occurs and to investigate the mechanisms responsible. To achieve this goal, Rydberg states must be created and allowed to interact with the desired

target surface while suffering minimal perturbation. The product ions must be detected, and the surface should remain stable. The apparatus employed is comprised of an interaction region, a metastable xenon source, a laser system, and control and data acquisition electronics.

Briefly, a beam of $6s'[1/2]_0$ xenon metastable atoms is directed onto the target surface at various angles of incidence inside a vacuum chamber maintained at a pressure of $\sim 10^{-9}$ *Torr*. Close to the surface, a fraction of these metastable atoms are excited to the desired Rydberg state using a crossed laser beam that can be tuned from $462 - 475$ *nm*. Excitation is performed in near-zero electric field. The laser allows precision spectroscopy and is frequency stabilized to permit the laser to be locked on resonance with the desired transition. The UHV environment allows the maintenance of a reproducible surface.

Near the target surface, the potential for the excited electron contains terms associated with the core ion, induced image charges, the applied DC electric field, and local surface fields. Together, these result in a potential barrier between the atom and surface. Ionization can occur through resonant tunneling through this barrier, or direct over-the-barrier passage if the height of the barrier is less than the energy of the electron. For this work, tunneling through the barrier is neglected. It is assumed that the tunneling rate is a step-function, jumping from zero to infinity when the height of the barrier falls below the energy of the atomic state. This over-the-barrier model adequately describes the interaction for most cases.

Once ionized, the resulting core is pulled to the surface by its own image charge, where it can be lost to Auger neutralization. To prevent this, an electric field of variable strength is applied perpendicular to the surface immediately following excitation. The applied fields must be limited to values below those sufficient to directly field-ionize the Rydberg atoms in vacuum. (This direct field-ionization however, can be used to determine the Rydberg atom production rate.) For applied fields below field ionization threshold ion production must be associated with atom-surface interactions (neglecting ionization caused by blackbody radiation). The surface ion signal is identified by a channel electron multiplier (channeltron) and allows measurement of the arrival time distribution, which also permits the velocity distribution of the metastable xenon beam to be examined. Arrival time gating can then be used to discriminate against charged particles not formed through surface interactions. The surface ion signal is measured as a function of applied field and is normalized to Rydberg atom production. Analysis of the resulting data allows for reasonable estimates of ionization distances and the strength of surface fields.

Chapter 2

Theory

The goal of this chapter is provide a theoretical description of the interaction between a xenon Rydberg atom and a nearby surface. Rydberg states are described together with various models of their evolution in electric fields.

2.1 Xenon Rydberg Atoms

2.1.1 Properties

As seen in Table 1.1, with increasing n Rydberg atom size and lifetime increase while electronic binding energy decreases. The large physical size means that the Rydberg electron experiences a nearly pure Coulomb potential. Thus, to first order, high-n states of all elements behave similarly. The large physical size and weak binding also implies that high-n states are sensitive to perturbations, the effects of which increase with n. The long lifetime allows the study of these interactions within a laboratory time frame. Thus Rydberg atoms provide a unique tool for probing the ionization process at conducting surfaces.

For a xenon Rydberg atom, electron coupling to the core is best described by a $j_c l$ coupling scheme [14]. The energy levels are denoted $nl[K]_J$, where n is the principal

quantum number and l is the orbital angular momentum of the excited electron. K is the vector sum of the orbital angular momentum, l, and the total angular momentum of the core, j_c, and J is the total angular momentum of the atom. For xenon, the valence electron is excited from a filled p-state. The core is left with $l_c = 1$ and $s_c = \pm 1/2$ and thus may have $j_c = 1/2$ or $3/2$. The state of the core is denoted $^2P_{1/2}$ or $^2P_{3/2}$, where the superscript indicates that the core is a spin-doublet. The orbital angular momentum of the excited electron is labeled l for the excited states with the lower energy core, $^2P_{3/2}$, and l' for the excited states with the higher energy core, $^2P_{1/2}$.

Single photon excitation from the ground state is not feasible due to the lack of a deep-UV photon source. As explained in greater detail in Chapter 3, the Xe(nf) Rydberg states employed here are created by photoexcitation of xenon $^3P_0$ metastable atoms created by electron-impact excitation in a DC discharge. This $6s'[1/2]_0$ state has energy 76196.79 cm^{-1} = 9.4472 eV [15] and a lifetime of 13 ms. As seen in Figure 2.1, two different Rydberg series can be produced by single photon excitation:

$$6s'[1/2]_0 \rightarrow n\mathrm{p}[1/2]_1 \tag{2.1}$$

$$n\mathrm{f}[3/2]_1 \tag{2.2}$$

Of these, the $6s'[1/2]_0 \rightarrow n$f transition was selected as the required wavelengths range from 462 – 487 nm. Single frequency laser light within this range is readily achievable with current laser technology. Such transitions have been observed and

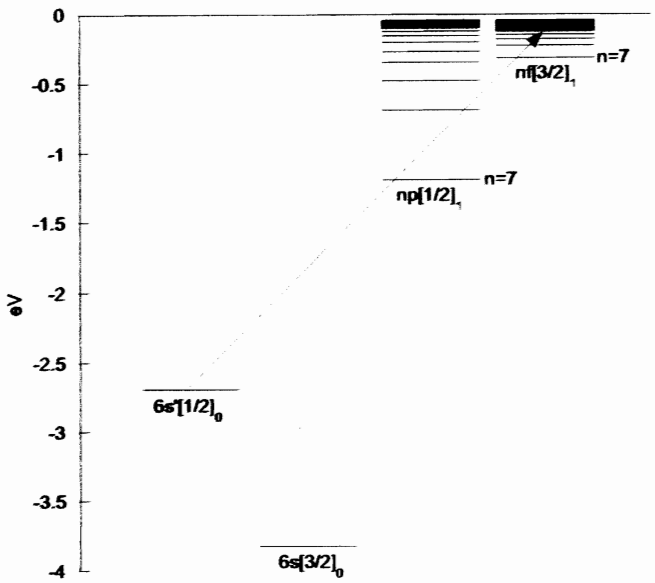

Figure 2.1 : Partial xenon energy diagram.

used to measure the energies of the Rydberg levels and to determine the quantum defects [16–18].

While the $j_c l$ coupling scheme best describes the individual atomic states, it does not entirely account for the allowed transitions. The selection rules in $j_c l$ coupling for electric-dipole transitions are $\Delta J = 0, \pm 1; \Delta K = 0, \pm 1; \Delta l = \pm 1; \Delta j_c = 0$. Both transition series given above violate the last selection rule while the $6s'[1/2]_0 \rightarrow nf$ transition also violates the $\Delta l = \pm 1$ selection rule. Knight and Wang [17] have attributed the existence of the $6s'[1/2]_0 \rightarrow nf$ transition to mixing of the $6s'[1/2]_0$ state with the $5d[1/2]_0$ state, with this d character permitting excitation to the nf states. Furthermore, the transitions to the $np[3/2]_1$ states are weak. Knight attributes

this to destructive interference between the 6s'→ np and the 5d→ np portions of the transition, though this has yet to be quantized.

As mentioned in section 1.1.1, the effects of core penetration and coupling are seen in the atomic energy levels. The binding energy of a Rydberg atom can be approximated by equation 1.2. The quantum defect interpolated by Haich [18] for f states, $\delta_f = 0.055$, yields binding energies ranging from $\sim$70 meV to $\sim$5.5 meV for n=14 and n=50, respectively. While the zero-field lifetime of the 50f state is $\sim$62.5 μs which is extremely long relative to the timescale of the experiment, the zero-field lifetime of 14f state is $\sim$1.4 μs which limits the time a Ryberg atom has to interact with the surface.

2.1.2 Behavior in Electric Fields

The sensitivity of Rydberg atoms to external electric fields is one of the underlying attributes that makes them both interesting and useful. Understanding the behavior of Xe(nf) Rydberg atoms in an electric field is critical to the work described here. As an introduction, consider a Hydrogen atom in the presence of an electric field F in the z direction. If the nucleus is centered at the origin then the potential experienced by an electron is given (in atomic units) by

$$V = -\frac{1}{r} + Fz \tag{2.3}$$

which has a saddle point on the z axis at $z_c = -1/\sqrt{F}$, as shown in Fig 2.2. At the saddle point the potential has the value $V_c = -2\sqrt{F}$. Therefore, if the electron is

bound by an energy E ionization will occur at fields greater than

$$F = \frac{E^2}{4} \tag{2.4}$$

Writing the binding energy as $E = -1/2n^2$ and substituting this value into Eq. 2.4 yields the classical ionization threshold in terms of the principal quantum number.

$$F = \frac{1}{16n^4} \tag{2.5}$$

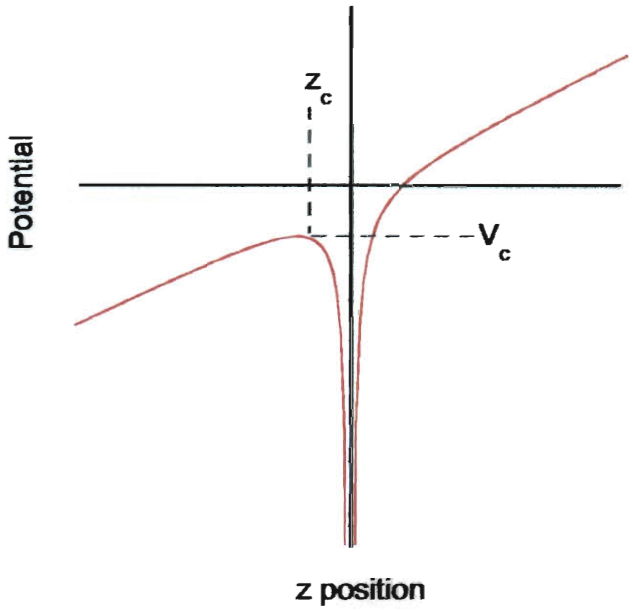

Figure 2.2 : Combined Coulomb-Stark potential experienced by an electron in a uniform field in the z direction.

In the presence of an electric field however, a given principal quantum number no longer defines a single energy. Each energy level splits into several Stark states [19]. In the presence of a field, l is no longer a good quantum number.

The addition of the linear term in the potential (Eq. 2.3) means that the Schrödinger equation is no longer separable in spherical coordinates. Fortunately, the Schrödinger equation separates in parabolic coordinates [19]:

$$\xi = r + z; \quad \eta = r - z; \quad \phi = tan^{-1}(y/x), \tag{2.6}$$

and the wavefunction can be expressed as a product of functions:

$$\Psi(\xi, \eta, \phi) = u_1(\xi) \cdot u_2(\eta) \cdot e^{i \cdot m_l \cdot \phi} \tag{2.7}$$

The resulting Eigenenergies depend on the principal quantum number n, the magnetic quantum number m_l, and two quantum numbers n_1 and n_2 which count the number of nodes in $u_1(\xi)$ and $u_2(\eta)$. Thus n_1 and n_2 are nonnegative integers and are related to n and m by

$$n = n_1 + n_2 + |m_\ell| + 1 \tag{2.8}$$

If a perturbation expansion is carried out using the zero-field wavefunctions, the first order correction to the energies is given by [19]

$$E = -\frac{1}{2n^2} + \frac{3}{2} \cdot F \cdot n(n_1 - n_2) \tag{2.9}$$

Figure 2.3 shows the Stark splitting of the energy levels in hydrogen as a function of applied field for $|m_\ell| = 1$. To a good approximation, the splitting is linear all the way to the point of field ionization. For the extreme red-shifted Stark state the shift causes an increase in the binding energy, which for $m = 0$ is adequately given by

$$E = -\frac{1}{2n^2} - \frac{3}{2} \cdot n^2 \cdot F \tag{2.10}$$

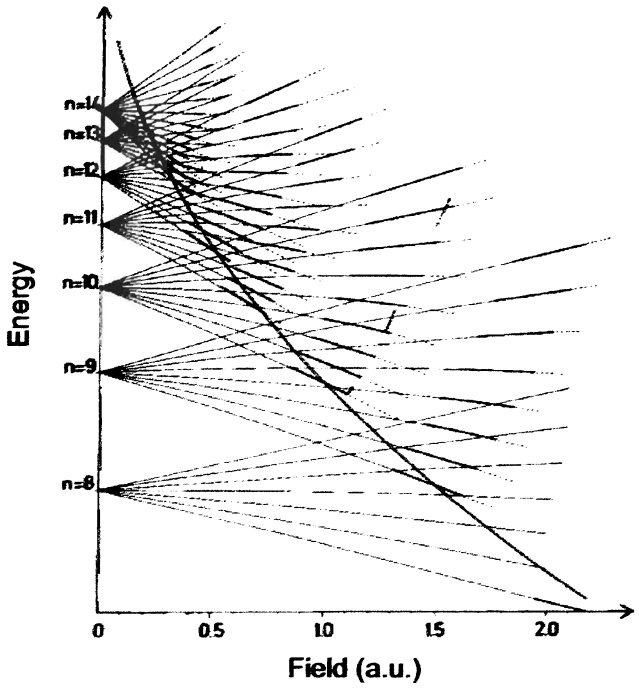

Figure 2.3 : Stark structure of the hydrogen atom for the $|m| = 1$ states. The broken lines indicate where ionization begins to occur. The solid heavy line represents the $E = -2\sqrt{F}$ saddle point [9].

Setting this equal to the potential at the saddle point, $V_c = -2\sqrt{F}$, one sees that the resulting threshold field for this state is

$$F = \frac{1}{9n^4} \tag{2.11}$$

Comparing this to the classical ionization threshold (Eq. 2.5), we see that the Stark shift of the energy level increases the numerical factor from 1/16 to 1/9.

The energy shifts expressed in Eq. 2.9 are associated with the classical dipole moment of the atom interacting with the electric field. The state with the largest

dipole moment that is antiparallel to the field is highest in energy ($n_1 - n_2 = 7$ in Fig. 2.4) and the state with the largest dipole moment parallel to the field is lowest in energy ($n_1 - n_2 = -7$ in Fig. 2.4).

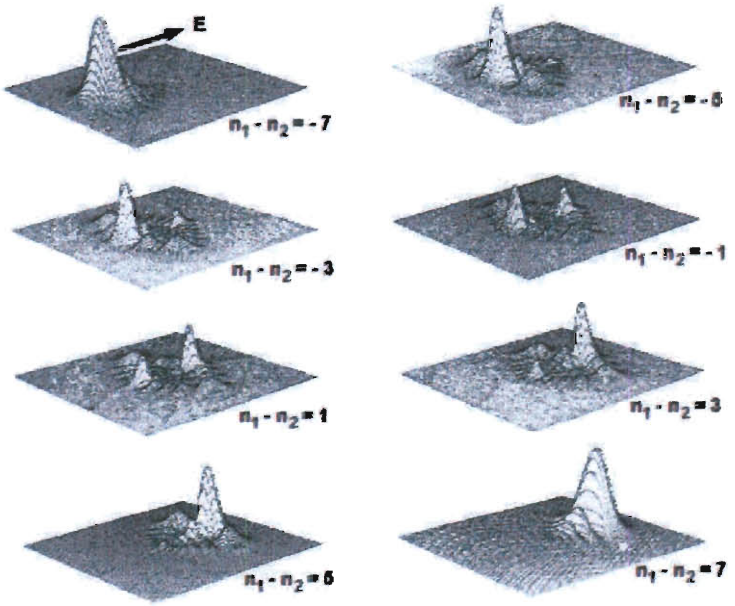

Figure 2.4 : Hydrogenic charge distributions for n=8 Stark states in an electric field [19].

However, hydrogenic theory fails to fully describe the complexity of the interaction between a xenon Rydberg atom and an electric field. Core interactions induce coupling between neighboring Stark states which strongly perturb these energy levels and eigenfunctions. To take this into account, Oubre [20] employed an angular momentum dependent pseudopotential for the xenon Rydberg core ion. This pseudopotential is

described by:

$$V^{PS}(r) = (\sum_{l} V_l^{PS}(r) \cdot |\, l >< l\,|) - \frac{1}{r} \tag{2.12}$$

where r is the radial coordinate. Following Bardsley [21], the pseudopotentials $V^{PS}(r)$ are assumed to have the form:

$$V^{PS}(r) = A_l \cdot r^P \cdot e^{(\xi r^q)} - \frac{\alpha_d}{2(r^2+d^2)^2} - \frac{\alpha_q}{2(r^3+d^2)^3} \tag{2.13}$$

where $\alpha_d = 4.044\ a.u.$ and $\alpha_q = 14.235\ a.u.$ [22] are the dipole and quadrapole polarizabilities, $d = 1.0\ a.u.$ is the cutoff distance, and the parameter ξ was set to 0.01. The coefficients A_l were determined by fitting the calculated atomic energy levels to those measured experimentally [23, 24]. The wavefunctions were expanded in a basis consisting of generalized Laguerre Polynomials and spherical harmonics [25]:

$$\phi_{nlm} = e^{-\lambda r/2} \cdot r^l \cdot L_n^{2l+2}(\lambda r) \cdot Y_{lm}(\Omega) \tag{2.14}$$

where the parameter $\lambda = 0.25\ a.u.$ was chosen to optimize the basis set. The total number of basis functions used was 600.

Using this potential, evolution of the energy levels becomes much more complex than for hydrogen. As the field increases Stark states for neighboring n-levels converge, and eventually overlap. This is know as the Inglis-Teller limit, and as can easily by shown using Eq. 2.9, The field corresponding to the first overlap is given by

$$F \cong \frac{1}{3n^5} \tag{2.15}$$

Due to the coupling induced by core interactions the states do not actually cross, but

instead suffer an avoided crossing. The level separation is described by a magnitude ω_o, as illustrated in Fig. 2.5, and is larger for low-$|m|$ states.

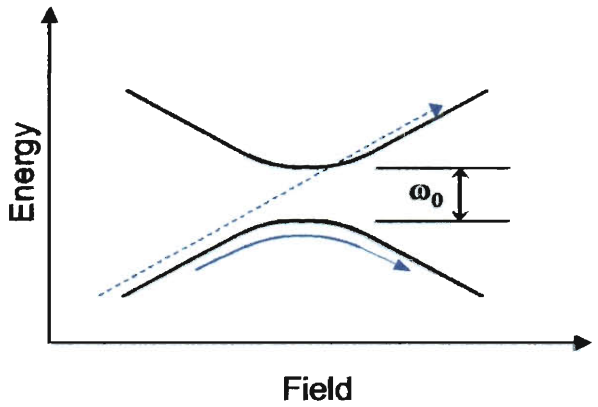

Figure 2.5 : Stark levels at an avoided crossing ω_o showing adiabatic (solid arrow) and diabatic (broken arrow) passage.

If the applied field is slewed through the crossing on a time scale that is long when compared to $1/\omega_o$ the electron wavefunction will have sufficient opportunity to adjust to the changing fields and passage through the avoided crossing will be adiabatic. At each avoided crossing the atom will pass smoothly from one Stark state into another until ionization occurs. If, however, the electric field is applied quickly compared to $1/\omega_o$, then the electron wavefunction will not have sufficient time to evolve from one state to another. The passage through the avoided crossings will then be diabatic, and the atom will remain in the same Stark state until the point of ionization. The avoided crossings for xenon m=0 states in the vicinity of n=14 are shown in Fig. 2.6.

Behavior in the region of these avoided crossings is of particular interest here.

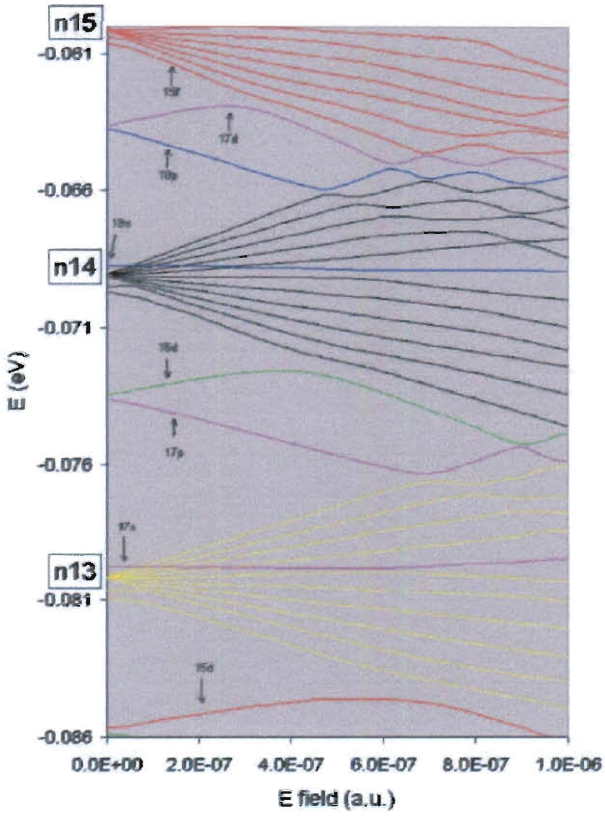

Figure 2.6 : m=0 Stark structure for xenon near n=14 [26].

Contour plots of the electron probability densities, $|\Psi(\rho, z)|^2$, for the lowest state in the n=15, m=0 Stark manifold (which correlates to the zero-field 15f state), and the highest Stark state for the neighboring n=14 manifold are shown in Fig. 2.7 for a DC field of 500 $Vcm^{-1} = 9.723 \times 10^{-10}$ $a.u.$ As one would expect based on Fig. 2.4, these states have very different spatial characteristics. The downward or red-shifted 15f state is strongly oriented along the $-z$ axis, whereas the upward or blue-shifted state

is strongly oriented along the $+z$ axis. The correlation between the spatial orientation of these states and their Stark energy shifts can be understood using simple classical arguments. For the case of the red-shifted (blue-shifted) state, the induced atomic dipole moment, $\vec{p}$, is parallel (antiparallel) to the externally applied electric field, $\vec{E}$, and the associated potential energy, $-\vec{p} \cdot \vec{E}$, is negative (positive).

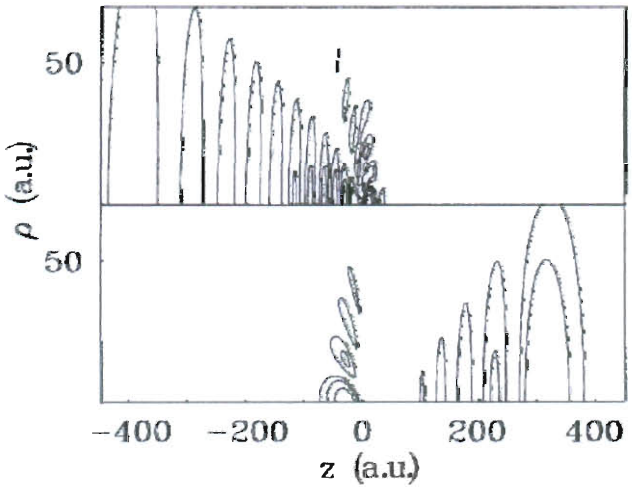

Figure 2.7 : Xenon electron probability contour plots for lowest state in the $n = 15$ manifold (top) and highest state in the n=14 manifold (bottom) in a 500 Vcm^{-1} field oriented along the $+z$ axis [26].

2.1.3 Interaction with Conducting Surfaces

Earlier approaches to modeling the interaction between Rydberg atoms and conducting surfaces focused on the resonant-ionization model. In this model, it is assumed that as the atom approaches the surface, wavefunction overlap between the electron

and the surface increases, increasing the likelihood of the electron tunneling to the surface. Chaplik [27] developed the earliest estimates for ionization distances by employing a hydrogenic model and adding perturbation terms associated with image charge interactions to the Hamiltonian. These perturbation terms, however, were only valid if the atom-surface separation was much larger than the size of the classical Rydberg atom.

Later, Wille [28] attempted to calculate the atom-surface separation at which ionization occurred. However, these calculations neglected the perturbation to the excited electron's orbit by it's own image charge, and hence were also inadequate. More recently, non-purturbative calculations for hydrogen were undertaken by Nordlander and Dunning [29–31] as well as by Küprick [32] and Nedeljković [33] which employed the complex scaling and etelon equation methods, respectively. These calculations predicted ionization rates which increase exponentially as the atom approaches the surface [34]:

$$\Gamma(z) = \Gamma_o \cdot e^{-\frac{z(1-kE_o)}{Z_{dec}}} \tag{2.16}$$

where z is the atom-surface separation, $E_o \equiv n^4 E$ is the ion collection field scaled to n, and Γ_o, Z_{dec}, and k are constants.

Early attempts to explain xenon Rydberg-atom surface interactions using this model [34–36] were able to successfully fit experimental data, however the decay lengths needed were hundreds of atomic units, as opposed to the tens of atomic units predicted by hydrogenic theory. In fact, the required decay lengths were so large that

they predicted a change in ionization rate of $1/e$ over length scales on the order of the size of the atom or larger, which was not physically reasonable. Furthermore, studies carried out at varying angles of incidence (thus modifying the component of velocity towards the surface and changing the energetics involved) required different ionization rates to fit the data for each angle [3], thus the model was not self-consistent.

The calculations which had been undertaken to attempt to determine ionization distances or ionization rates up to this point had all hinged on a fundamental assumption; that the surface employed was a perfect conductor and hence at a uniform potential. While this is certainly true macroscopically, crystal-defects, grain-structure and impurities call into question whether or not this assumption is valid microscopically. In the present work, we examine Rydberg atom-surface interactions under the assumption that the surface potential is *non*-uniform. As will be detailed in the following chapters, a simple over-the-barrier model adequately describes the interactions when the stray fields on the surfaces employed are taken into account.

Chapter 3

Experimental Apparatus

This chapter provides a detailed description of the present experimental apparatus. As noted earlier, the apparatus is comprised of four primary elements: the main vacuum chamber and interaction region, the metastable xenon source, the laser system, and the control and data acquisition electronics.

3.1 Vacuum System and Interaction Region

The present vacuum system is divided into three chambers. The first chamber houses the metastable source where the metastable xenon atoms are formed and roughly collimated. The second chamber houses a gas cell which allows for characterization of the metastable beam. The third and final chamber houses the main interaction region, which contains the final slit aperture, the target surface, wire meshes used to apply the DC electric fields, and a charged particle detector. A schematic of the apparatus can be seen in Figure 3.1

The source and intermediate chambers are each pumped by a 900 $L \cdot s^{-1}$ Varian 6" diffusion pump. A water baffle separates these chambers from the pumps allowing base pressures of 5×10^{-8} *Torr*, as measured by nude Bayard-Alpert type ionization gauges in each chamber. The source and intermediate chambers are separated

by a 0.025" aperture in an aluminum skimmer through which the metastable beam emerges.

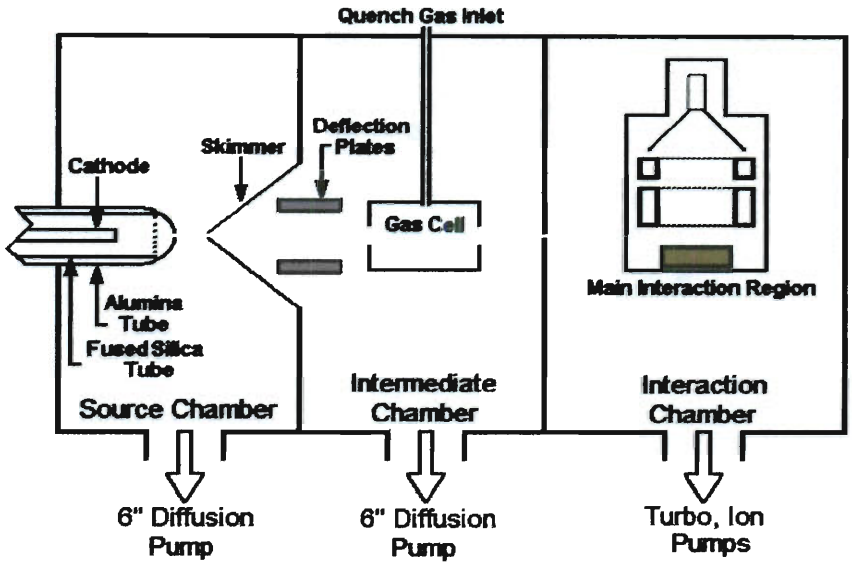

Figure 3.1 : Schematic diagram of the experimental apparatus.

The final chamber is pumped by a 450 $L \cdot s^{-1}$ Balzers TPU tubomolecular pump which maintains a base pressure of $\sim 10^{-9}$ $Torr$. A 400 $L \cdot s^{-1}$ Perkin Elmer ion pump is also attached which allows for base pressures of $\sim 10^{-11}$ $Torr$ after baking. The final chamber is separated from the intermediate chamber by a 0.100" diameter aperture which further collimates the beam of metastable atoms leaving the skimmer. The final chamber can be isolated from intermediate chamber using a gate valve.

The final chamber houses the main interaction region, a schematic of which is presented in Figure 3.2. A laser-drilled 80 μm (0.003") slit aperture provides the

final collimation of the incident beam of metastable xenon atoms. The interaction region is fixed to a 360° rotatable flange whose rotation axis is near the center of the target surface. All components are electrically isolated allowing bias voltages to be applied or signals measured.

The metastable beam impacts the target surface at a shallow angle defined by the position of the slit aperture (the uncertainty in incident angle which results from the range of possible impact points along the target surface is about $\pm 0.5°$ for a 4° incident angle). The laser beam enters the interaction region parallel to the target surface and perpendicular to the metastable beam. The laser beam position can be adjusted via a lens on a translation mount to allow Rydberg excitation at various points along the metastable beam, and hence at various distances from the target surface.

Voltages are applied to a series of 70 *line/inch*, 90% optically transparent grids to establish electric fields above the surface and to accelerate ions towards the charged particle detector. The three grid assembly has a total transmission of 73%. The nearest of the three grids is 0.200" (5.08 *mm*) from the target surface. A voltage pulse of controlled amplitude is applied to the two grids nearest the surface to establish the ion collection field. The amplitude of this pulse is the fundamental experimental variable, allowing the investigation of atom surface interactions in a variety of applied fields or, if the pulse is sufficiently large, allowing direct field-ionization of the atoms before they can interact with the surface permitting determination of the Rydberg

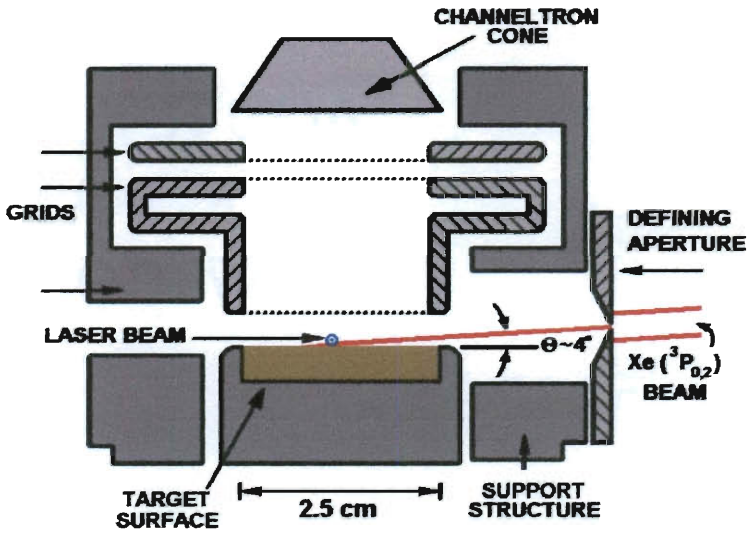

Figure 3.2 : Schematic diagram of the main interaction region.

atom production rate.

The third grid is biased to the same potential as the input of a charged-particle detector. This voltage gives control of the impact-energy of the Xe^+ ions allowing the detection efficiency to reach saturation. The detector is a Dr. Sjuts channel electron multiplier (CEM or channeltron). The channeltron also requires a second bias voltage which controls the potential gradient across the gain channel. This voltage allows the channeltron gain to be controlled and check than it is sufficient to achieve saturation.. The channeltron was operated with a front voltage, $V_{chf} = -3\ kV$ and a back voltage, $V_{chb} = -500\ V$ giving a $\Delta V = 2.5\ kV$ accross the gain channel.

3.2 Metastable Xenon Source

Metastable xenon atoms are excited via electron-impact excitation of ground-state xenon atoms in a plasma contained in a supersonic expansion. A schematic of the metastable xenon source assembly is shown in Figure 3.3. A detailed description of the different types of metastable sources, the theory describing them, and the motivation for choosing a supersonic DC discharge, are given elsewhere [37,38].

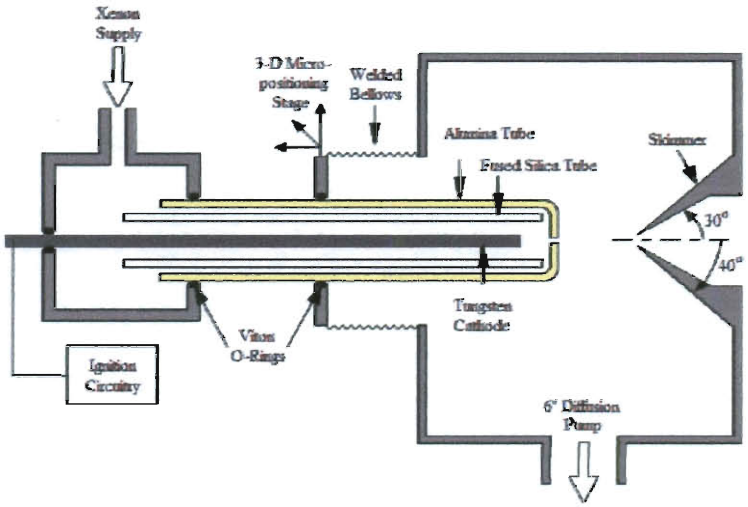

Figure 3.3 : Schematic diagram of the metastable xenon source assembly.

99.995% pure atomic xenon is admitted into an alumina tube and unergoes supersonic expansion into vacuum through a 0.007" laser-drilled aperture at its end. A discharge is ignited between the 0.125" tungsten cathode and the 0.025" diameter aperture of the aluminum skimmer. The fused silica tube prevents the discharge from

lighting between the cathode and sputtered tungsten on the inner wall of the alumina tube.

Figure 3.4 shows the electrical schematic of the DC discharge. The cathode is biased negative to accelerate any positive ions toward the alumina tube and not down the beam line. The cathode housing is mounted to the chamber via an accordion-type welded bellows and a 3-D micro-positioning stage. The position of the alumina tube relative to the skimmer aperture can be fine tuned allowing for proper alignment and spacing of the tube.

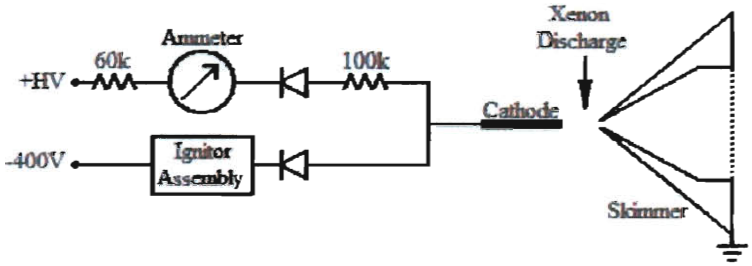

Figure 3.4 : Electrical schematic diagram of the metastable xenon source.

The physics of DC discharges in general is not well understood. When the discharge is lit it behaves as a negative resistance; the resistance decreasing as the current increases. Thus to stabilize the discharge a large series resistance is employed. The source has been characterized previously [3], and parameters permitting stable operation determined. The data presented here were obtained at a source chamber pressure of $\sim 8.5 \times 10^{-5}$ *Torr* and an applied high voltage of 1750 V.

3.3 Laser System

The wavelength required to excite some of the Rydberg levels used in the present work from the Xe($^3P_0$) metastable level are given in Table 3.1. The Rydberg states were originally excited using light produced by a UV-pumped Coherent 899-21 Coumarin-47 dye laser. Difficulties with the UV pump laser and the short dye lifetime made this approach problematic. Because of this, a switch was made to an extracavity-doubled titanium:sapphire laser. This system utilized a Coherent Innova-400 Argon Ion laser operating at 514.5 *nm* to pump a Coherent 899-21 titanium:sapphire ring laser. The resulting IR output was then doubled using a Coherent MBD-200 frequency doubler.

To eliminate issues associated with a fairly short lifespan of the Innova-400 laser tube, the Argon Ion pump laser was replaced with a Coherent Verdi 18 *Watt* laser. The new solid-state pump laser delivers a TEM_{00} mode, and since it requires no tuning, provides a much more position-stable pump beam for the titanium:sapphire laser. The V-18 is typically operated at $\sim$ 16.5 *Watts*, further increases in power begin to cause thermal lensing in the titanium:sapphire crystal which results in reduced stability. This solid-state pump laser was used in the acquisition of the data presented here.

3.3.1 Pump Laser

The Verdi V-18 laser system is a compact, solid-state diode-pumped, frequency doubled Nd:Vanadate (Nd:YVO_4) laser which provides single-frequency green (532 *nm*)

output in a TEM_{00} mode. This system is comprised of several laser diodes operating at 1064 *nm*, which are coupled to an optical fiber. The fiber passes light to the head-assembly, in which an LBO crystal doubles the frequency providing the 532 *nm* light.

Light originates from 38 individual laser-diodes. The laser diodes are arranged into two fiber array packages (FAPs), each containing 19 diodes. In each FAP, the diodes are arranged concentrically around a central optical fiber. Typically ~90% of the emitted light is transmitted to the optical fibers.

The fibers carry light into the head assembly, which is a hermetically sealed laser cavity utilizing Vanadate as the gain medium and LBO as the frequency doubling crystal. The laser head also employs an etalon and an optical diode in the 4-mirror cavity to ensure unidirectional single-frequency lasing. The temperatures of the etalon and Vanadate crystal are controlled via thermo-electric coolers, which can either heat or cool the components. The LBO crystal is non-critically phase matched and is held at ~150°C by a resistive heater. The entire laser head assembly rests on a baseplate which is cooled by a chilled-water system.

3.3.2 Titanium:Sapphire Laser

The Verdi-18 pump laser provides 16.5 *Watts* output at 532 *nm* in the TEM_{00} mode. This is focused into the titanium:sapphire crystal to induce population inversion of the embedded $3d^1$ Ti^{3+} titanium ions from the $^2T_2$ ground state to the ^2E excited

stated, as illustrated in Figure 3.5. The titanium sapphire laser is known as a vibronic laser due to closely spaced vibrational and electronic energy levels of the titanium ion that broaden the available lasing modes.

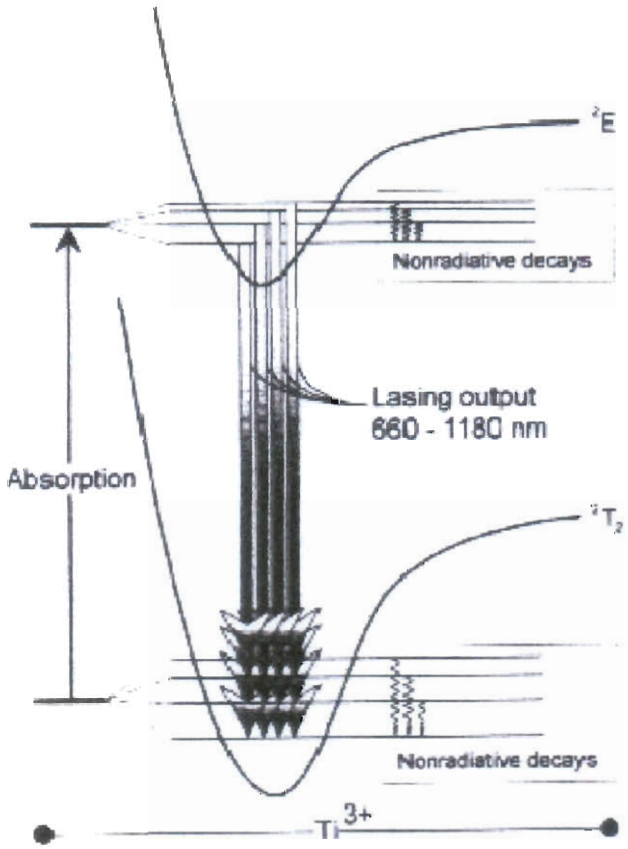

Figure 3.5 : Diagram of titanium:sapphire energy levels.

The laser cavity in its current configuration is shown in Figure 3.6. Single frequency operation in accomplished using a 3-plate birefringent filter with a passive bandwidth of 380 GHz, a thin etalon with a 200 GHz free spectral range, and a

thick etalon with a 10 GHz free spectral range. These elements allow for tuning through the lasing range in 10 GHz wide steps with an effective line width of <500 kHz. Scanning within a single 10 GHz step is achieved electronically via integrated control servos. Conversion efficiencies vary widely from a few percent to better than 10%, over the tuning range which extends from 600 - 1200 nm. Specially coated optics optimized for operation at different wavelengths within this range are available. The current optics are coated for wavelengths from $\sim$ 900 - 1200 nm.

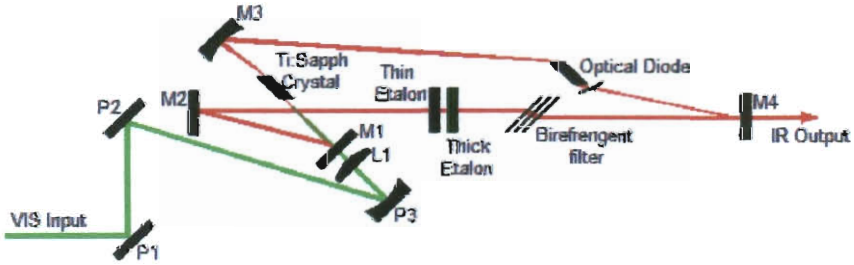

Figure 3.6 : Diagram of the CR-899-21 Ti:Sapph laser.

The the titanium:sapphire laser allowed single-wavelength outputs spanning ~940 nm down to ~890 nm. This allowed for excitation of n-levels from $n = 17$ up to the ionization limit. There was an abrupt fall off in the maximum lockable power observed near 940 nm. Upon investigation, it was determined that the instability resulted from a malfunction of the optical diode. It is perhaps more appropriate to consider this malfunction a design flaw, as the assumption that an optical diode designed for visible wavelengths will function properly at IR wavelengths is not 100% correct.

The optical diode uses two polarization rotating elements, a Faraday rotator which rotates polarization about a magnetic field, and an optical rotator which rotates polarization about the direction of propagation. If these rotations are matched, then light traveling in the forward direction experiences the difference in rotation (i.e. zero) while light traveling in the reverse direction experiences the sum (non-zero). Both Faraday rotation and optical rotation, to first order, fall off with respect to the square of the wavelength. This $1/\lambda^2$ dependence causes the optical diode to be less effective at longer wavelengths since light traveling in the reverse direction experiences less polarization rotation and hence less reflective loss at each Brewster-cut interface. Beyond 940 *nm* the rotation of the linear polarization provided by the optical diode could not provide sufficient differential gain to suppress reverse-lasing. The quartz crystal which, together with a magnet assembly, comprises the Faraday rotator was replaced with a TGG crystal which provides more than an order of magnitude more rotation in the same B-field. The new Faraday rotator assembly was placed in the beam line, and its rotation was measured to be 10.25° at ~930 *nm*, a tremendous improvement to the <0.5° of the original Faraday rotator. An optical rotator was cut to give an identical rotation at the same wavelength. These new optics were placed in the cavity on a custom mount which allowed optimization of their tilt-angles. Stable operation has been achieved using the new optical diode assembly at wavelengths as long as 955 *nm*. Stable operation at longer wavelengths may be possible, but other components (namely the 3-plate birefringence filter, or BRF) limit the power and

stability.

3.3.3 Wavelength Measurement

A small portion (~5 %) of the IR output of the titanium:sapphire laser is directed toward a scanning Michelson interferometer seen in Figure 3.7. The IR beam is aligned collinear with the ouput of a polarization-stabilized He-Ne laser. Each beam is split and sent along two paths on either side of a scanning cart optic. Thus as the cart scans back and forth, one path will increase in length, and the other will decrease by an identical amount. The beams emerging from the two paths are then superimposed on one another and incident on two photodiodes (one for the He-Ne and one for the IR). This results in alternating "fringes" of constructive and destructive interfence as the cart tracks back and forth. The number of fringes is given by:

$$N = \frac{d}{\lambda} \tag{3.1}$$

where λ is the wavelength, and d is the length of the track. Since both wavelengths travel identical path lengths, the wavelength of the unknown IR light can thus be computed by:

$$\lambda_{Unk} = \frac{n_{He-Ne}}{n_{Unk}} \cdot \frac{N_{He-Ne}}{N_{Unk}} \cdot \lambda_{He-Ne} \tag{3.2}$$

where n_{He-Ne} and n_{Unk} are the refractive indices for each laser in air and N_{He-Ne} and N_{Unk} are then number of fringes counted for each laser. A track length of ~2 *feet* constitutes about a ± 1 GHz (± 0.01 Å) error in the wavelength measurement across visible and IR spectrum. Corrections for the index of refraction change from

the IR to the Blue were taken from the 2002 CRC values. The interferometer allows the titanium:sapphire laser to be tuned typically within 500 MHz of the required atomic transition frequencies.

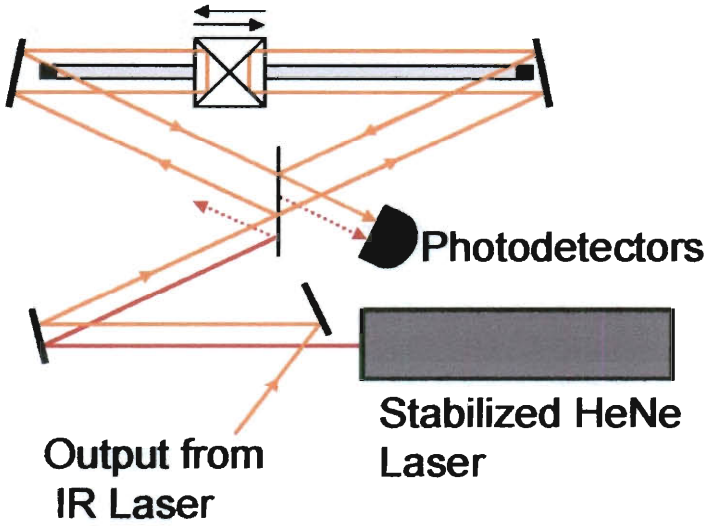

Figure 3.7 : Scanning Michelson interferometer.

3.3.4 Frequency Doubler

The IR output of the 899-21 is focused into a MBD-200 extracavity doubler which uses a Lithium Triborate (LBO) crystal as the nonlinear medium. Harmonic conversion yields the 460-475 nm light necessary to excite the required Xe(nf) Rydberg states. The LBO crystal is critically phase-matched and is cut for optimum phase matching at 945 nm. The conversion efficiency is rated at 10%/$Watt$. A half-wave plate allows

for a small rotation of linear polarization of the incoming light. This introduces a small orthogonal component, which due to the birefringence of the LBO crystal, is not on resonance with the cavity. These two polarization components back-reflect and are fed into a system of locking photodiodes. This is known as the Hansch-Couillaud active resonator stabilization technique, and is used to lock the size of the frequency doubling cavity on resonance with the fundamental (IR) wavelength. This allows the resonant cavity to track small frequency changes of the input laser. A schematic of the doubler is shown in Figure 3.8

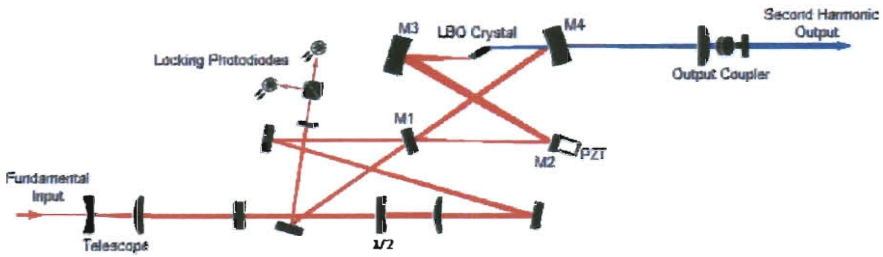

Figure 3.8 : Schematic Diagram of the MBD-200 frequency doubler.

Due to the second harmonic generation process, the spacial output mode from the MBD-200 is highly elliptical. Using a spherical and cylindrical lenses, the beam is shaped so that at the intersection with the xenon metastable beam the beam size is $\sim$ 250 $\times$ 200 μm at the 1/e width. The beam is apertured at several stages to produce a near TEM_{00} mode at this point [3]. The output is vertically polarized.

The CW output of the MBD-200 is chopped into a train of pulses of $\sim$ 1 μs duration by passing it through an acousto-optic modulator (AOM) before it enters

the interaction region. The AOM consists of a PZT transducer mounted to a fused quartz block and is operated as a Bragg device. The transducer generates a traveling RF acoustic wave within the glass resulting in a periodic variation in the refractive index. This produces a diffraction grating which deflects up to 90% of the input light out of the zero-order. This allows the vast majority of the laser light to be deflected to the first order electronically. Thus the first-order output can be pulsed with a precise width and repetition rate.

3.3.5 Frequency Stabilization

A small portion ($\sim$ 5%) of the blue frequency-doubled light is picked off before the AOM. This light is directed onto a polarizing beam splitting cube. The output from a second polarization-stabilized He-Ne laser is directed onto an adjacent face of the polarizing beam splitter. The He-Ne is polarized horizontally, hence it travels straight through the cube, while the vertically polarized blue light reflects 90°, superimposing the two beams. Both beams then travel through a thermally stabilized, scanning Fabry-Perot interferometer. The Fabry-Perot cavity is driven by $\sim 1\ kV$ ramp applied to a PZT crystal which scans the rear mirror of the cavity at a repetition rate of $\sim$ 30 Hz. Light is transmitted when the cavity length allows for the formation of standing waves. He-Ne and Blue contributions are separated by another polarizing beam splitter. The transmitted red and blue light are sent to two photodiodes. The voltage separation between the red and blue transmission peaks, illustrated in

Figure 3.9, are monitored and held constant by providing a feedback signal to the titanium:sapphire laser. This external locking scheme known as "superlock" improves on the $\sim$ 100 MHz/hr drift inherent to the 899-21 by limiting the drift to $\sim$ 1 MHz/day, which is the specified drift of the polarization stabilized He-Ne laser. The superlock system also allows for an external offset allowing precise scanning of the blue light over a range of $\sim$ 300 MHz

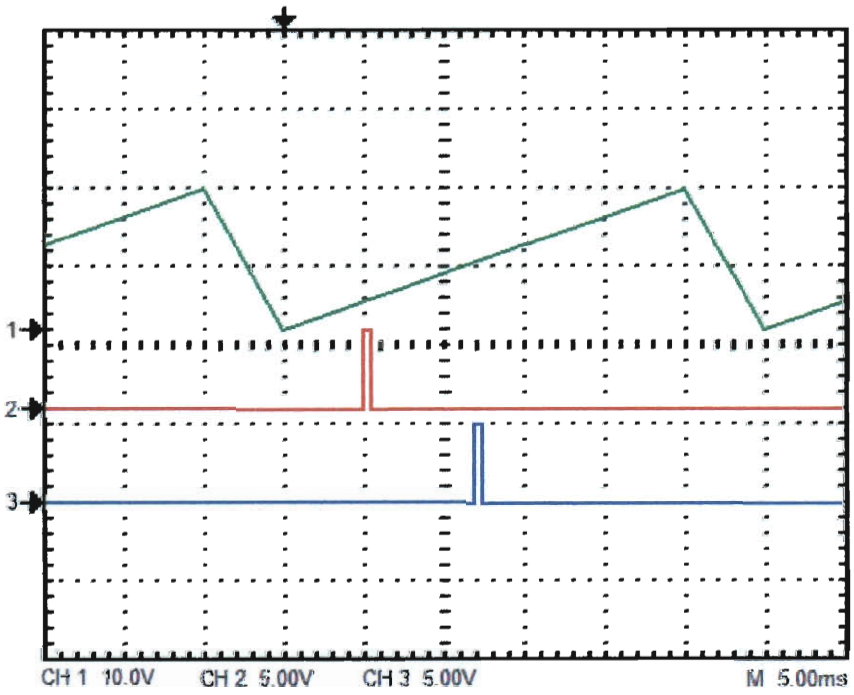

Figure 3.9 : Superlock ramp and photodiode signals.

3.4 Control and Data Acquisition Electronics

The electronics required to drive the apparatus are comprised of two CPUs, several pulse and delay generators, numerous power supplies, and other miscellaneous circuits and devices. A general schematic is shown in Figure 3.10. The blue boxed region represents the optics and laser assemblies, the purple boxed region represents the xenon source assembly, the green boxed region represents the interaction region, and the red boxed region represents the control and data acquisition electronics.

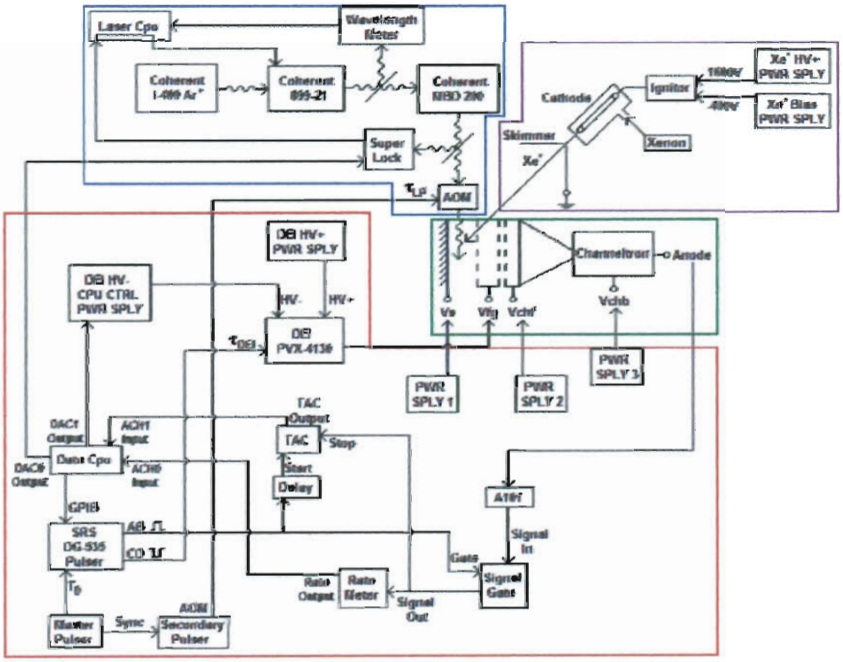

Figure 3.10 : Experimental schematic.

The time base is set by a master pulser which defines the repetition rate for the experiment, typically 3 - 4 kHz. This pulser outputs a TTL pulse which triggers

the computer controlled SRS DG-535 pulser and also synchronizes a secondary pulse generator. The secondary pulser is a simple square-wave generator of variable width and delay that drives the AOM, thus setting the time and width of the laser pulse, τ_{LP}. The SRS pulser is controlled via data acquisition programs using a GPIB PCI interface. The SRS has two channels of arbitrary width and delay. One is used to trigger DEI PVX-4130 pulser, while the second is used to gate the pulse counting electronics, allowing discrimination of the various signals observed.

The data acquisition control computer allows for external scanning of the 899-21 titanium:sapphire laser either by providing an offset to the superlock system or by controlling the offset of the 899-21 directly. The analog output to the external frequency control of the 899-21 is accurate to 100 kHz. A second analog output voltage controls a Glassman FC series power supply allowing the voltage used to generate the ion collection field to be stepped from ground to field-ionization in as little as 5 V steps. this voltage is fed to a DEI PVX-4130 voltage pulser. The DEI is effectively a high-voltage, solid-state relay which can switch up to 6 kV in as little as a few nanoseconds. For all work presented here, the rise time was slowed to $\sim$1 μs using a simple RC network to limit switch-noise pickup and to ensure that all avoided crossings between Stark states are traversed adiabatically.

The signal from the channeltron is tested by a threshold detector based on an Analog Devices A101 chip, and the resulting pulses are sent to a gating circuit. If the gate voltage for signal collection is high, the detector pulses are passed to an Ortec

ratemeter which integrates the total number of pulses during a preset time base. The ratemeter outputs an analog voltage between 0 and 10 V for zero and max-scale count rates, respectively. This analog output is read by the data acquisition computer at the end of each timing cycle. The gated detector pulses are also sent to an Ortec 566 Time to Amplitude Converter (TAC). The TAC outputs a voltage pulse proportional to the time between a detector pulse and a start pulse set by the signal gate. This allows for measurement of ion flight time distributions.

The data acquisition computer is a Pentium 4, 2.6 GHz chip on an Intel D875PBZ mainboard with 1 GB of RAM running windows XP professional. LabView 7.1 software handles the interfacing of the input and output signals via a PCI-6036E series data acquisition card and the previously mentioned GPIB interface. Specific LabView based programs have been developed to allow for scanning of the laser, application of the field pulses, and synchronized recording of the input and output data. These programs are synchronized to the master pulse through the SRS DG-535 pulser.

For lifetime measurements presented in this work, a second DEI pulser was used to apply a positive voltage to the target surface. Since both SRS channels were already in use, an adjustable TTL RC delay generator was fabricated allowing the signal gate to open $\sim$1 μs after the second DEI was switched on. This allowed the timing of both DEI pulse generators to be computer-controlled, while maintaining the ability to employ arrival time gating.

n-level	λ-literature [23,39]	λ-interpolated	λ-measured
10	487.134	487.105	
11	482.583	482.579	
12	479.191	479.193	
13	476.585	476.592	
14	474.536	474.548	474.552
15	472.900	472.913	472.913
16	471.573	471.583	
17	470.468	470.486	470.485
18	469.556	469.572	
19	468.786	468.801	
20	468.121	468.144	468.143
21	467.556	467.581	
26		465.683	465.684
27		465.425	465.426
28		465.195	465.195
30		464.802	464.803

Table 3.1 : $6s'[1/2]_0 \rightarrow nf$ transition wavelengths for selected states from n=10 to n=30.

Chapter 4

Experimental Methods

This chapter provides a detailed description of the methods used in examining the ionization of Rydberg atoms incident at varying angles on conductive surfaces. It will provide a complete description of the experimental parameters and protocols.

4.1 Excitation of Xe(nf) Rydberg Atoms

The first experiments concerned the excitation of the desired Xe(nf) Rydberg states. These were done using a 1 - 5 μs laser pulse followed by a $\sim$ 20 μs field-ionization pulse. The timing arrangement is seen in the oscilloscope traces seen in Figure 4.1. Channel 1 designates the laser pulse, τ_{LP}, channel 2 designates the signal gate, τ_G, and channel 3 designates the field ionization pulse, τ_{DEI}. A delay of $\sim$ 1.5 μs between the end of the laser pulse and the start of the field ionization pulse accounts for delays inherent in the AOM.

Classically, the field necessary for direct field ionization is $1/16n^4$ $a.u.$. The measured field ionization threshold for the Xe(20f) Rydberg state is $\sim$ 2400 $V \cdot cm^{-1}$ ($4.5 \cdot 10^{-7}$ $a.u.$). The xenon excitation spectrum for the 20f state is shown in Figure 4.2, other n-levels are similar. Excitation was performed in a DC field of $\sim 5\ V \cdot cm^{-1}$ with a 1 μs laser pulse.

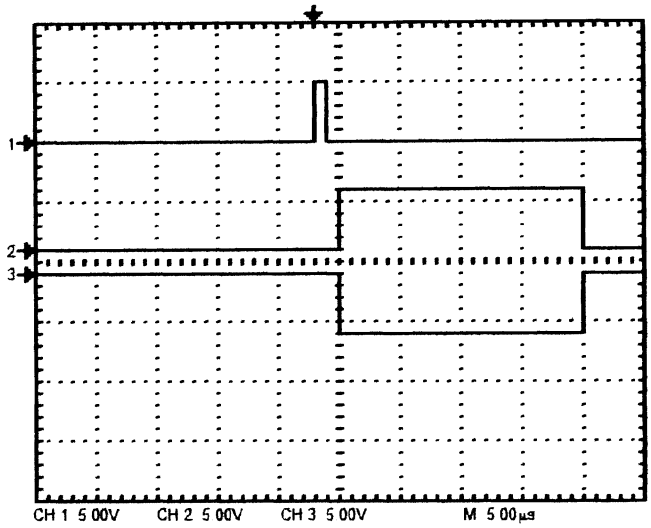

Figure 4.1 : Pulse timing For Rydberg atom excitation and field-ion detection.

The observed spectrum is quite complex, primarily due to the nine stable isotopes of xenon. The features seen have been attributed (from left to right) to the ^{136}Xe, ^{134}Xe, ^{132}Xe, ^{130}Xe, ^{128}Xe, ^{126}Xe, ^{136}Xe and ^{124}Xe isotopes. The ^{131}Xe and ^{129}Xe isotopes are outside the scan range [3]. The ^{130}Xe and ^{128}Xe isotopes are closely spaced, but easily resolved. The second factor which contributes to the complexity of the observed excitation spectrum is hyperfine structure.

The hyperfine splitting of a transition is affected by the interaction between the non-spherically symmetric charge distribution in the nucleus and the non-spherically symmetric electric field produced by the atomic electrons. Further complicating the matter are the different charge distributions in the nucleus for each isotope. Similar complex spectra have been observed by Walhout [40].

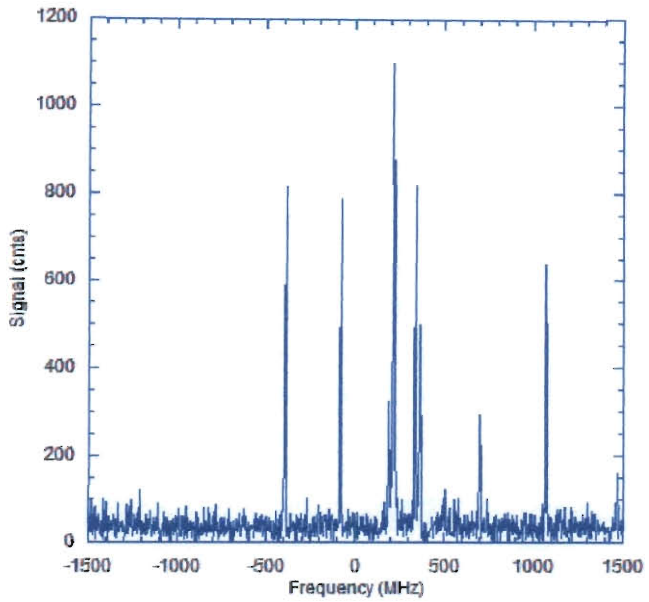

Figure 4.2 : 3 GHz frequency scan of Xe(20f) Rydberg states.

When necessary, the Rydberg states are excited in a small DC electric field in order to remove any zero-field degeneracy and to allow for selective excitation of the lower-most (i.e. red-shifted) states within the Stark manifold. Figure 4.3 shows the excitation spectra for the Xe(20f) state in several weak DC electric fields. The leftmost peak, representing the ^{136}Xe isotope, shows no splitting. It can easily be seen from the 12.5 V/cm curve however, that the ^{134}Xe isotope (the second isotope) is split into three states. The 25 V/cm curve shows the same effect, but is confused by the presence of additional peaks from the ^{132}Xe isotope. More in-depth studies of the degenerate states are presented in Section 4.4.2. For all data presented in this

work, the ^{136}Xe isotope isotope was used due to it being the most abundant of the isotopes which are non-degenerate in zero-field.

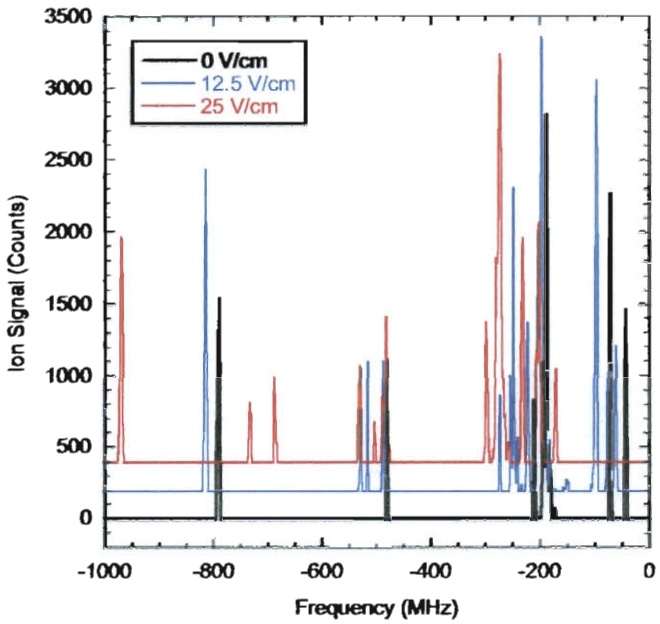

Figure 4.3 : N=20 excitation spectra in weak DC electric fields.

4.2 Surface Ion Arrival Time Distributions

4.2.1 Position Calibration

The position of the laser beam governs the flight time of a Rydberg atom to the target surface. As the laser beam is brought closer to surface, the Rydberg atoms arrive at the surface sooner relative to the time of excitation, hence the surface ion signal is seen earlier in the arrival time distribution. Eventually the laser beam will

be eclipsed by the target surface and the surface ion signal will be lost. A typical arrival time distribution is presented in Figure 4.4 for n=20 Rydberg atoms incident at 4.5° relative to the target surface with an applied field of 2 $kV \cdot cm^{-1}$ and with excitation occurring approximately 4.5 mm up the beam line from the surface (~350 μm above the target surface).

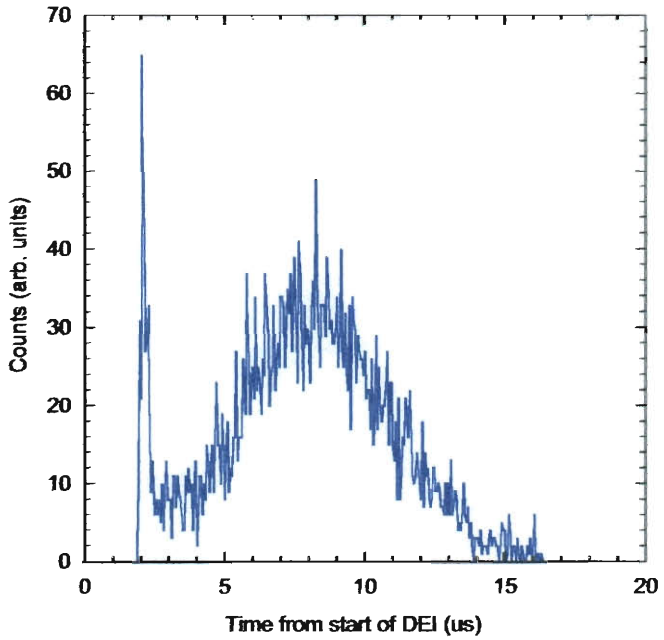

Figure 4.4 : Typical surface ion arrival time distribution.

Two features are immediately apparent. The first is a sharp peak at $\sim 2\ \mu s$. This fast spurious signal will be analyzed in more detail in Section 4.2.2. The second feature is a broad peak resulting from Rydberg atoms which must travel to the surface in order to ionize before being pulled to the detector by the collection field. This signal

results from Rydberg atom-surface interactions, and can easily be distinguished from other signals with arrival time gating.

To this end, the most desirable running condition is achieved when the crossing point is far enough from the surface that the total surface ion signal is well distinguished from the early arrival signal, but no further out than necessary to resolve the two signals. This position minimizes the number of atoms lost to radiative decay, and hence minimizes inaccuracies introduced when a correction is made for this decay, but still allows for arrival time gating. Typically, this position results in an average surface ion arrival time of ~ 7 - 8 μs.

4.2.2 Early Arrival Signal Characterization

The early arrival signal was originally attributed purely to photo-ions [3]. Due to the arrival time gating employed, this signal is resolved from the surface ion signal. However, when the Rydberg atom production rate is measured via direct field ionization, *all* ion signals arrive immediately after the field is applied. Thus the early arrival signal is present in the measured Rydberg atom production rate, and the resulting collected fraction will be slightly lower. In order to minimize this inaccuracy, the early arrival signal was studied in the hopes of minimizing or eliminating it.

A key observation was the fact that the early arrival signal decreased, and eventually vanished as n was increased, or more importantly, as the critical field required for ionization was reduced. The fact that certain applied fields were too weak to

contribute an early arrival signal is inconsistent with photo-ions since any ions far from the surface would be immediately pulled towards the detector by the application of extremely weak fields. Since it was obvious that the early arrival signal was *not* due to ionized atoms, it was suspected that it was due to high-n Rydberg atoms created in the DC discharge via electron impact excitation. Rydberg atoms have been known to be a product of electron impact excitation for decades [41–44]. Freund *et al* have observed Rydberg states in electron impact spectra of several atoms and molecules [45–48].

An attempt was made to ionize the Rydberg atoms in the metastable xenon beam using a strong transverse DC electric field. A set of deflection plates in the beam line were re-purposed to accomplish this, and the field across them was set to the maximum value sustainable without inducing coronal discharge. The voltages employed were $\sim 500\ V$ and -2 kV. Count rate measurements were made with the laser off, ensuring that no Rydberg atoms were created via single-photon excitation. The measurements with and without the transverse field applied to the metastable xenon beam are shown in Figure 4.5.

Inferring information about the distribution of Rydberg states in the metastable xenon beam from this data is difficult, due to the fact that the deflection plates are not parallel, giving a range of electric field strengths across the beam. Also, the various Rydberg states have radically different zero-field lifetimes for radiative-decay, ranging from very short for low n-levels to very long for high ones. The lifetimes will also

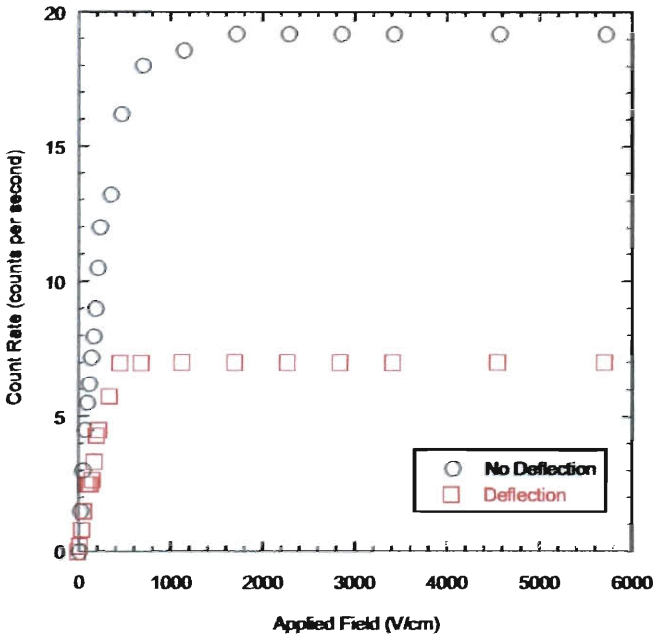

Figure 4.5 : Background count rate vs applied field with and without a transverse field applied to the metastable beam.

depend on the orbital quantum number, l. This, coupled with a flight time of about a millisecond, greatly affects the likelihood of a given Rydberg atom surviving passage to the interaction region. Nonetheless, it is obvious that the spurious early arrival signal is due (at least primarily) to atoms which are ionized by the applied field, and not to photo-ions. Also, the data show that a DC electric field across the metastable beam can reduce the number of Rydberg atoms created in the discharge which survive passage to the interaction region by a factor of ~ 3. The voltages specified were applied to the deflection plates during the acquisition of all data presented here.

4.2.3 Gate Timing Determination

Another factor governing the arrival time distribution is strength of the applied ion collection field. For weaker fields, the ions are accelerated toward the detector more slowly leading to later arrival times of both the surface ion signal and the early arrival signal. Thus the timing for the signal gate must change with the ion collection field. For collection fields above $\sim$ 1.5 $kV \cdot cm^{-1}$ the flight time from the surface to the detector is $\lesssim$ 1 μs, and further increases in collection field strength will not have a noticeable impact on the arrival time distributions.

In order to establish appropriate signal gate timings for a given laser beam position, surface ion arrival time distributions are measured in 100 - 200 V increments starting with the lowest collection field for which a surface ion signal is seen, up to 1.5 kV or the critical field for ionization, whichever comes first for the n-level under investigation. From each distribution, the midpoint between the fall of the early arrival signal and the start of the surface ion signal is chosen to open the signal gate.

4.3 Field Dependent Lifetime Measurement

An electron in an excited state, nl, will spontaneously decay to a lower lying state, $n'l'$. The spontaneous decay rate from the excited state, nl, to the lower lying state, $n'l'$ is given by the Einstein A coefficient and can be written as [49]

$$A_{n'l'} = \frac{4e^2\omega_{nl,n'l'}^3}{3\hbar c^3}\frac{l_{max}}{2l+1}|<n'l'|r|nl>|^2 \tag{4.1}$$

The radiative lifetime, τ_{nl}, of the excited state is simply the inverse of the total radiative decay rate summed over all lower lying $n'l'$ states

$$\tau_{nl} = \left[\sum_{n'l'} A_{n'l',nl} \right]^{-1} \tag{4.2}$$

The factor of ω^3 in Eq. 4.1 suggests that the transitions with the highest frequencies will contribute the most to the radiative decay rate and therefore dominate the overall n dependence. For high nl states, as $n \rightarrow \infty$ the frequency of the highest transitions becomes constant [9]. The Einstein A coefficient value then only depends on the radial matrix element between the nl state and the lower $n'l'$ state. The only contributing factor within the radial matrix element is the fraction of the nl state's wavefunction which overlaps that of the lower $n'l'$ state. The squared matrix element exhibits n^{-3} scaling due to normalization and thus

$$\tau_{nl} \ \alpha \ n^3 \tag{4.3}$$

The field dependent lifetimes for n=17 and n=20 have been measured previously [3], and for $n \geq 26$, the radiative lifetimes were found to be long relative to the time scale of the experiment, hence radiative decay was negligible. However, a detailed measurement of radiative lifetimes was conducted for n=14.

The laser beam was moved to a position far from the surface, such that excited atoms experienced a long flight time ($\sim$ 10 μs) before interacting with the surface. Immediately following excitation, the desired external field was applied to the Rydberg atoms via a positive voltage, $V1$, pulse on the target surface. The number

of Rydberg atoms surviving at a later time was measured by applying a negative voltage, $-V2$, pulse to the first mesh, such that the difference, $V1$ - (-$V2$), gives an electric field which is 10% greater than the critical field for ionization ($\sim$ 10 kV for n=14).

The maximum voltage which could be applied to the surface was insufficient to field ionize n=14 atoms, so once the voltage applied to the surface reached 2.5 kV, the order of the pulses was reversed. In this new configuration, the negative pulse applied to the mesh established the applied field, and the positive pulse to the target surface provided the remaining portion of the total voltage difference needed to achieve field ionization.

With the number surviving at a time, τ, known, this number was then normalized to the production rate determined by direct field ionization immediately after excitation to give the fraction surviving at time τ. This measurement was then repeated for several values of τ from 0 to 6 μs, and the exponential decay rate found via exponential curve-fitting. A few representative curves are shown in Figure 4.6

A similar curve was measured for all applied fields between 0 $V \cdot cm^{-1}$ and the critical field for ionization in $\sim$ 50 $V \cdot cm^{-1}$ steps, and the lifetimes determined from exponential fits. The resulting lifetimes are shown in Figure 4.7.

The reasons for employing such a small field step are immediately apparent as the lifetime varies greatly and non-monotonically of the range of applied fields. This will be discussed further in later chapters.

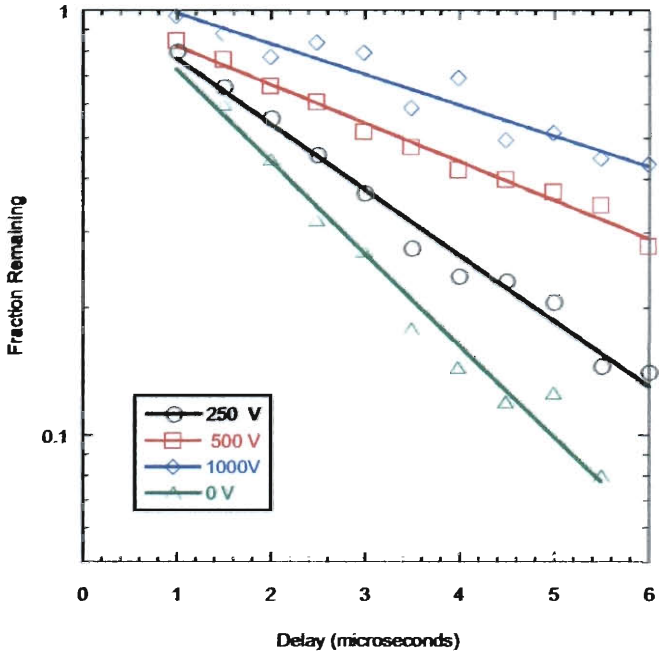

Figure 4.6 : Fraction surviving Vs. delay for n=14 atoms in a several applied fields.

4.4 Ionization of Xenon Rydberg Atoms at Conductive Surfaces

4.4.1 Surface Ion Measurement

The surface ion signal is measured by the application of the ion collection field immediately following a $\sim$ 1 μs laser pulse. Any atoms which ionize sufficiently far from the surface for the ion collection field to dominate the image charge attraction towards the surface are accelerated to the channeltron. The resulting signal is gated as shown in the scope traces in Figure 4.8 in order to isolate the surface-ion signal.

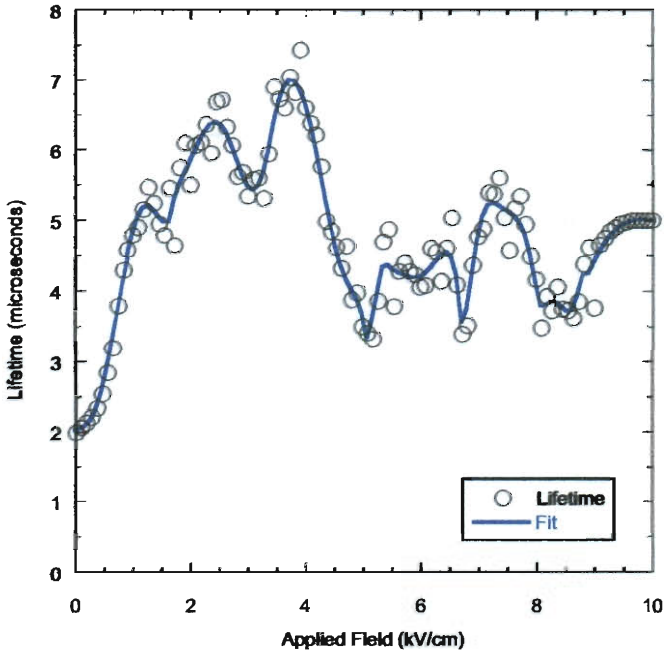

Figure 4.7 : Field dependent radiative lifetime for Xe(14f) Rydberg atoms.

The laser pulse is first applied (channel 1), followed by the application of the DC field (channel 3). The signal gate (channel 2) can be opened at an arbitrary delay time, after the spurious early-arrival signal has passed.

The laser is scanned across the desired transition of the chosen isotope rather than locked on resonance. While this reduces the net count rate, it makes the experiment insensitive to residual charge which might build up on a resistive surface. If the surface does not fully discharge before the application of the next laser pulse, the transition will be slightly Stark-shifted. Since the transition frequency can change with varying ion collection fields, scanning through the transition within a reasonably

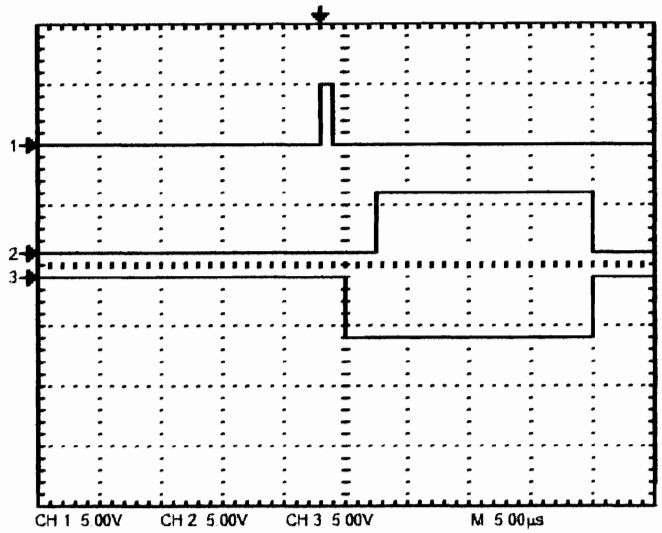

Figure 4.8 : Pulse timing for Rydberg atom excitation and surface-ion detection.

large frequency window (typically $\sim$ 30 MHz for a transition with $\sim$ 8 MHz full-width half-max) allows curve fitting algorithms to find the peak of the transition regardless of small frequency shifts.

To determine the fraction of surface ions collected, the Rydberg atom production rate must first be determined. This is accomplished by increasing the applied field above the threshold for ionization immediately after the laser pulse. The laser frequency is scanned across the transition and the ungated signal is taken to be the field-ionization signal. Typical frequency scans for field and surface ionization are shown in Figure 4.9 for n=20 Rydberg atoms in applied fields of 2.6 $kV \cdot cm^{-1}$ and 2 $kV \cdot cm^{-1}$, respectively, for atoms incident at 4.5° on Au(111). As can be seen, the field ionization scan results in a higher number of counts than the surface ionization

scan. This is partly due to radiative decay of the Rydberg atoms in transit to the target surface, and partly due to high-n Rydberg atoms for which the 2 $kV \cdot cm^{-1}$ applied field is sufficient for field-ionization. These ions are separated from the surface ion signal via arrival time gating, but are still present in the field-ion signal.

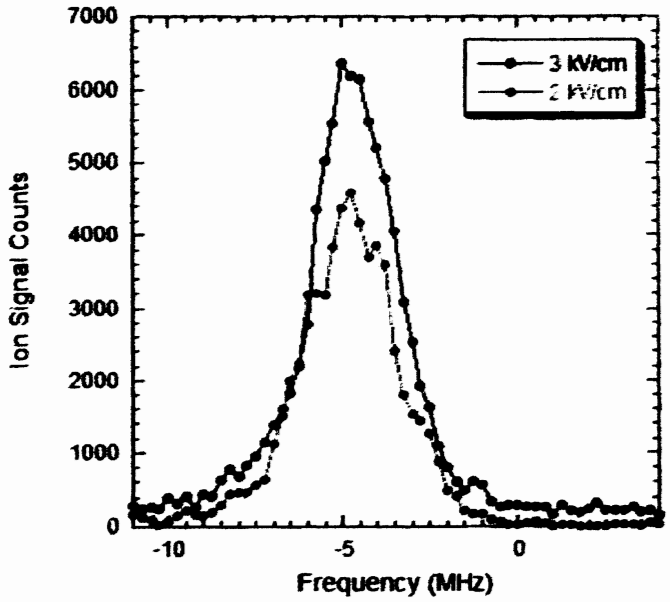

Figure 4.9 : Field and surface ionization frequency scans of the n=20 ^{136}Xe isotope.

At fields near, or exceeding field ionization, the early arrival signal is difficult to discriminate from the desired ion signal. This is best understood by considering the evolution of the arrival time distribution as the ion collection field is increased. Figure 4.10 shows arrival time distributions for several applied fields which are near the ionization threshold. As the applied field is increased, a portion of the atoms are observed to ionize immediately, and arrive coincident with the spurious early

arrival signal, while the remainder travel for some time towards the surface before ionizing. Some atoms may field-ionize in weaker fields than the rest due to significant contributions from surface fields, but a more likely explanation is non-uniformity in the applied field. The spacing between the surface and the first grid is less than the width of the target surface. Thus if the target surface, which is mounted to a sample holder with UHV compatible epoxy, is not affixed perfectly parallel with the grid, significant deviations in field can occur.

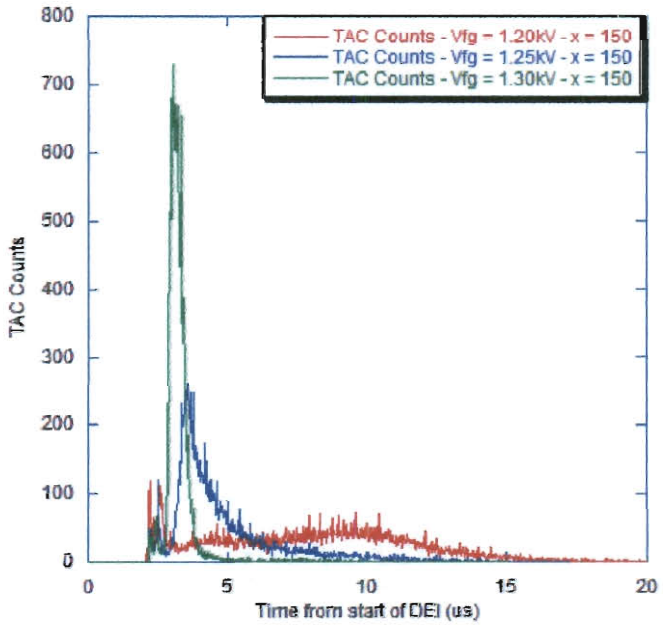

Figure 4.10 : Arrival time distributions for n=20 atoms incident at 4° in applied fields near the ionization threshold.

The frequency scan curves are then analyzed via three different curve-fitting algorithms. Two are Gaussian fits, one allowing a non-zero baseline and the other forcing

a baseline of zero, and the third is a splined polynomial fit. These three fits to the field ionization and surface ionization frequency scans allow the determination of five different collected fractions. For the two Gaussians, the ratio of the peak-heights is taken, as well as the ratio of the integrated areas. The ratio of the integrated area of the polynomial fit constitutes the fifth collected fraction. The peak height of the splined polynomial fit is not used, as it would only be sensitive to the number of ions collected at whichever specific laser frequency is determined to be the "peak".

While all five fractions are typically within $\sim$10%, it has been observed that the best reproducability and minimal scatter are observed using the peak-amplitudes of the non-zero baseline Gaussian fits. However, once the background count rate was drastically reduced with the application of the electric field across the metastable xenon beam, the collected fractions determined from the peak amplitudes of the zero baseline and non-zero baseline Gaussians agreed extremely well, typically within $\sim$1.5%. Nonetheless, to maintain consistency with historical data, the non-zero baseline amplitude was used to determine collection efficiencies for the data presented here.

This procedure of fitting frequency scans for field ionization and surface ionization is conducted for each applied ion collection field. Although each field ionization scan is performed under identical conditions and experimental parameters, repeating the scan for each applied field greatly reduces errors introduced by drifts in laser power or metastable xenon atom flux over the course of the data-run.

4.4.2 Degeneracy

With the procedure for determining ion collection efficiency vs. applied field described, it is worthwhile to revisit the question of degeneracy raised in Section 4.1. Figure 4.3 shows that if any zero-field degeneracy for the ^{136}Xe exists, the difference in energy of the different states is certainly less than the difference in energy for the ^{134}Xe states in a given field.

With each of the three states for ^{134}Xe easily resolvable, each could be studied independently and their effects on the resulting data analyzed. Surface ion collection efficiencies which are uncorrected for radiative decay are shown in Figure 4.11. As can be seen, the three curves saturate to slightly different values at high field strengths. However, the thresholds for ion collection and field ionization occur at essentially the same field strength for each state. This points to the fact while the three states have only small differences in energy, there may be some significant differences between the lifetimes of the three states.

Considering that the difference in energy between any possible zero-field degenerate states for ^{136}Xe is extremely small relative to ^{134}Xe and that the differences in energy between the three levels seen in the ^{134}Xe(20f) feature have a negligible impact on the experimental data, it is clear that the ^{136}Xe isotope can be considered to be non-degenerate. It is possible that multiple states with similar energies may be present in the ^{136}Xe(20f) level which may possess different lifetimes for radiative decay. This however should be accounted for, since the experimentally measured life-

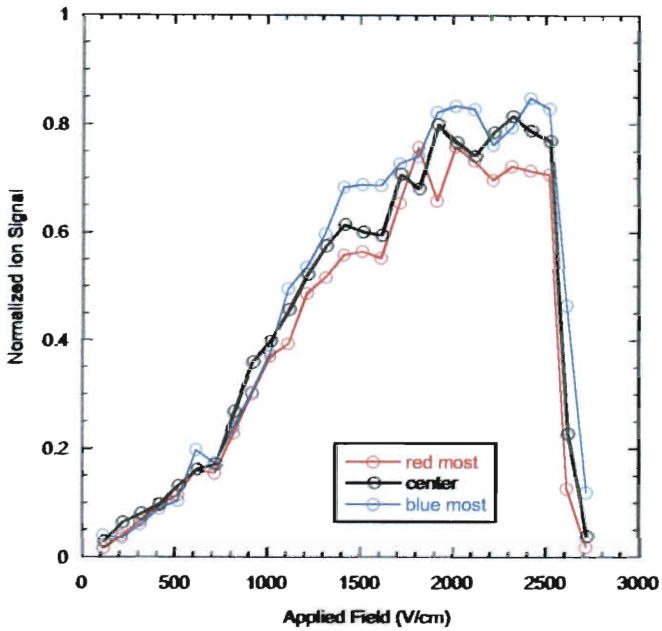

Figure 4.11 : Surface ion collection efficiencies vs. applied field for each of the three degenerate states of the ^{134}Xe(20f) state.

times for the ^{136}Xe(20f) state would be "effective" lifetimes, and the corrections for radiative decay would still be valid.

4.4.3 Velocity Distribution

The velocity distribution has been measured previously [3], but is of critical importance to this work. A first order velocity distribution was determined using arrival time distributions at various laser positions. This distribution, however, did not account for the fact that the 80 μm width of the metastable beam leads to Rydberg atom excitation over an 80 μm range of atom-surface separations, which results in

$\sim$1 mm range of distances to the surface at a 4° incident angle. Atoms excited closer to the surface have significantly shorter paths, and hence shorter flight times to the target surface than those excited further away. A Monte Carlo technique was used to account for the range of flight times associated with the various distances to the surface for different excitation positions in the metastable beam.

The velocity distribution for a supersonic expansion from a circular nozzle is expected to be a modified Maxwellian distribution [49]

$$f(\nu)\,\alpha\,\nu^3 e^{-\frac{m}{2k_B T}(\nu-\nu_0)^2} \tag{4.4}$$

Figure 4.12 shows the experimentally determined velocity distribution along with a fit generated using Eq. 4.4 with a beam energy of $\sim$10 meV and with $\nu_0 = 450\ m \cdot s^{-1}$. As seen from the figure, the modified Maxwellian velocity distribution is in excellent agreement with the velocity distribution determined experimentally.

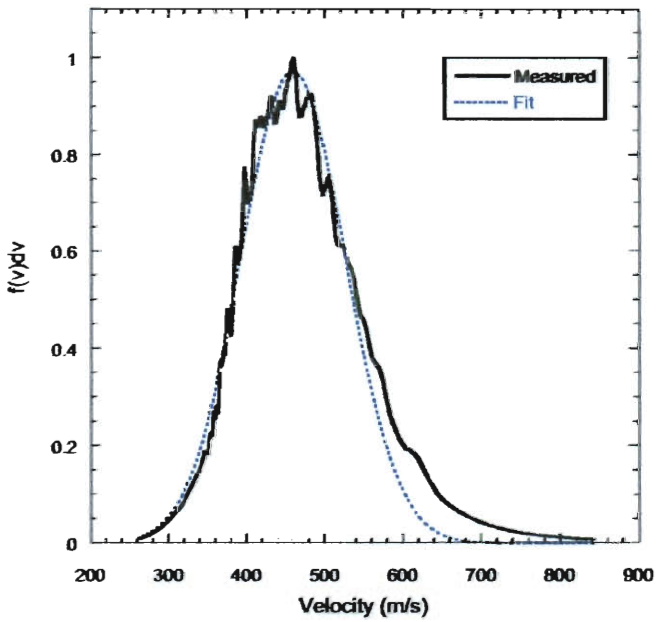

Figure 4.12 : Modified Maxwellian vs. experimentally determined velocity distribution.

Chapter 5

Data and Analysis Using The Monte Carlo Model

All analysis presented here will assume a simple over-the-barrier model. It is perhaps best to first consider the simplest possible case of a Rydberg atom positioned over an ideal plane conducting surface. Assuming the surface is at z=0, the electron is at position z, the core is at position Z, and in an applied electric field, F, the electron potential is given by

$$V(z) = -\frac{1}{|z-Z|} - \left(\frac{1}{4z} - \frac{1}{4Z}\right) + \left(\frac{1}{z+Z} - \frac{1}{2Z}\right) + F \cdot (Z-z) \qquad (5.1)$$

where the terms represent potentials due to Coulomb attraction, the electron image charge, the core image charge, and the applied field, respectively. Figure 5.1 shows the contributions to the electron potential from the core ion, the image charges, and a 1 $kV \cdot cm^{-1}$ applied field, as well as the total electron potential for a core-ion located 2000 atomic units from the surface. The binding energy of an n=20 Rydberg atom is shown for reference.

This figure clearly illustrates the potential barrier that lies between the core and the surface. The over-the-barrier model assumes ionization will occur whenever the height of the potential barrier is less than the binding energy of the Rydberg electron. In other words, the ionization rate is is assumed to jump from zero to infinity as the

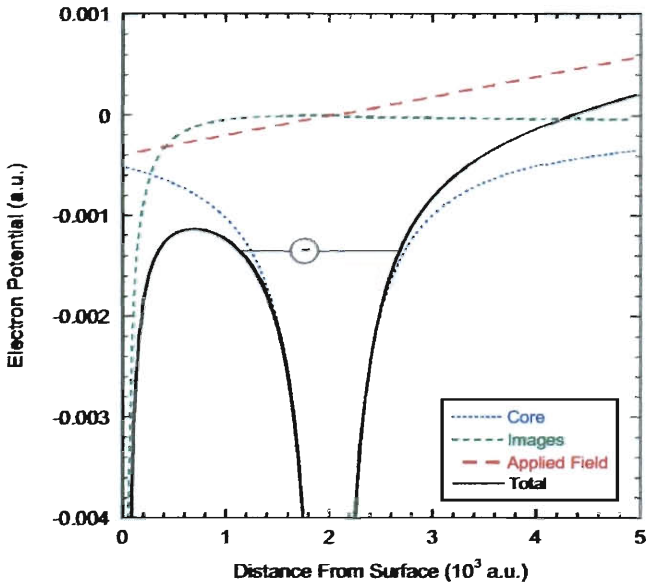

Figure 5.1 : Various electron potential contributions and total potential vs Z over an equipotential surface.

height of the barrer falls below the binding energy of the electron. As Figure 5.1 shows, the height of the barrier can be modified through a change in applied field, or through a change in core position via the Coulomb and image potentials.

A typical data set showing surface ion collection efficiencies vs applied field for n=20 atoms incident on a Au(111) surface at 4.5° is presented in Figure 5.2. This figure also presents the expected collection efficiencies for an ideal surface. Eq. 5.1 would indicate that all atoms will ionize at identical atom-surface separations, thus the resulting collection efficiency is a step function, but which is slightly broadened due to the range of atomic velocities.

In order to ensure that the observed broadening was not due to the topography of

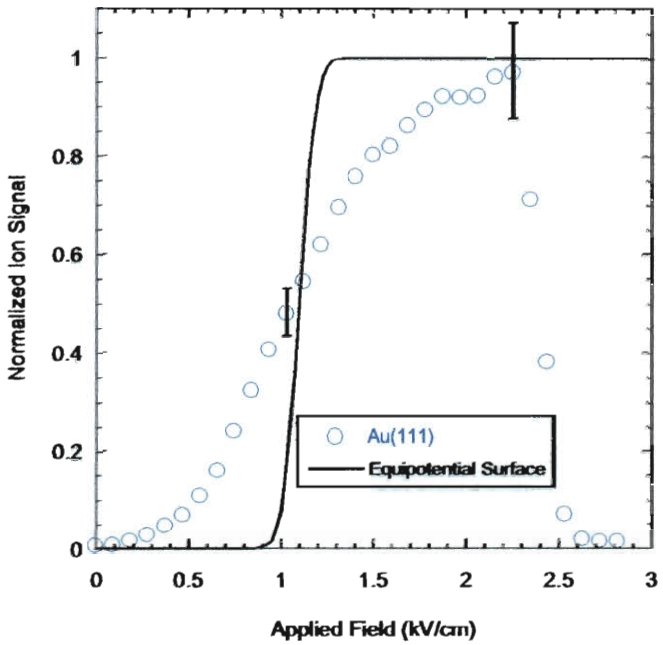

Figure 5.2 : Collection efficiencies vs. applied field for n=20 atoms incident at 4.5° and expected collection efficiencies for an equipotential surface.

the Au(111) target surface, a template stripping technique [50] was employed. The technique exploits the <4% compressive lattice mismatch between cleaved muscovite mica and Au(111) [51]. The Au surface which was evaporated onto mica was affixed to a sample holder with UHV compatible epoxy applied to the gold. The mica was then peeled off layer-by-layer using sticky-tape. Even though mica is transparent, it was not difficult to discern when the last mica layer was removed. Thin film interference can be obseved in the mica layers when viewed from the correct angle, and the presence of additional mica layers can easily be confirmed with an Ohm-meter. The evaporated surfaces typically display an RMS roughness $\lesssim$10 nm. Since cleaved

mica is actually a 2-dimensional crystal and one of the flattest known materials, a template-stripped Au(111) surface typically has a roughness <3 Å. Experimental studies of several n-levels using a template stripped target surface were found to provide identical results to those performed on the evaporated surfaces, indicating that surface topography of the scale present in an evaporated Au(111) surface was not a factor in the experimentally observed broadening.

The data indicate that using an over-the-barrier model, an ideal surface does not account for the experimental observations. The remainder of this chapter will illustrate that potential variations on the the target surface also modify the potential barrier, as well as affect the collection efficiency at a given ionization distance. This chapter will present the techniques for implementing a real surface potential into a Monte Carlo simulation utilizing the simple over-the-barrier model.

Previous approaches to modeling the Rydberg-atom surface interactions involved using an ionization rate and integrating over the known velocity distribution to determine collected fractions. While this approach was mathematically elegant and computationally inexpensive, it is impossible to implement such a model on a non-uniform surface. Even if the range of ionization distances could be determined by integrating over the entire surface, the results the surface fields would have on the collection of the ions would still need to be accounted for. It was determined that the simplest approach to modeling behavior above a non-uniform surface potential was to use Monte Carlo techniques

The Monte Carlo simulation has been previously presented in various stages of its development [1–3, 52]. Essentially, it acts as a virtual experiment by creating virtual atoms, using a simple over-the-model to determine where they will ionize, and numerically solving the ion's equations of motion to determine if the virtual ions are lost to the surface or if they escape far enough from the surface to ensure detection. The Monte Carlo simulation is capable of outputting collection efficiencies for various applied fields, allowing for direct comparison with experimental data.

5.1 Algorithm

5.1.1 Simulated Au(111) Surface

In order for the simulation to determine realistic ionization distances, a realistic model of the target surface is necessary. Early simulations [1,2] employed a chosen periodic surface potential, and made use of SimIon, a commercial software package utilizing the finite-difference (or "relaxation") method to numerically solve Laplace's equation and output data tables for either potential or electric field. One drawback to this approach was that memory limitations constrained the potential and electric field data to two dimensions. Translational symmetry was assumed in the third dimension. The 2-D periodic potential used thus effectively represented a surface of infinitely long wires.

Although this approach did offer a single, self-consistent set of parameters which could adequately predict experimental data for n=17 and n=20 at all incident angles studied, it could not demonstrate with certainty that surface fields were in fact re-

sponsible for the experimental observations. In order to justify the claim that surface fields were the cause of the observed broadening of the experimental data, the potential on the Au(111) surface was measured using Kelvin probe-force microscopy [53,54]. The potential measured by the atomic force microscope was first calibrated by applying a several large bias voltages (100 - 1000 mV) to a Au sample and observing the resulting average potential measured. This allowed for fine tuning of the gain settings on the lock-in amplifier used to measure the surface potential, in order to ensure an accurate quantitative surface potential measurement.

With the tool properly calibrated, the potential on a Au(111) surface was measured. The surfaces employed were purchased commercially, and were fabricated by evaporating gold onto freshly cleaved mica followed by annealing in a hydrogen flame. The surface potential measurements were performed over $1\mu m \times 1\mu m$ area using 512 $\times$ 512 sample points. This potential was then used as a boundary condition for Laplace's equation

$$\frac{\partial^2\phi}{\partial x^2} + \frac{\partial^2\phi}{\partial y^2} + \frac{\partial^2\phi}{\partial z^2} = 0 \tag{5.2}$$

in order to determine the potential at any point above the surface. Separation of variables shows that Eq. 5.2 is satisfied, for $z>0$, by linear combinations of periodic functions of the form [55]

$$\phi(x,y,z) = \sum_i \sum_j \left[A_{i,j} cos(k_{x,i}x + k_{y,j}y) + B_{i,j} sin(k_{x,i}x + k_{y,j}y)\right] e^{-k_z(i,j)z} \tag{5.3}$$

where $k_z(i,j) = \sqrt{k_{x,i}^2 + k_{y,j}^2}$. This potential is simply the Fourier expansion of the measured surface potential. Since the measured surface potential was stored as an

array of discreet points, the Fourier coefficients, $A_{i,j}$ and $B_{i,j}$, must be determined using a discreet 2-D Fourier transform with coefficients given by

$$A_{i,j} = \frac{2}{N^2} \sum_{m=0}^{N-1} \sum_{n=0}^{N-1} \phi\left(\frac{mL}{N}, \frac{nL}{N}, 0\right) \cos\left[\frac{2\pi(mi+nj)}{N}\right]$$

$$B_{i,j} = \frac{2}{N^2} \sum_{m=0}^{N-1} \sum_{n=0}^{N-1} \phi\left(\frac{mL}{N}, \frac{nL}{N}, 0\right) \sin\left[\frac{2\pi(mi+nj)}{N}\right] \tag{5.4}$$

for a surface potential assumed to be periodic over an $L \times L$ area ($1\mu m \times 1\mu m$ here) and represented by an $N \times N$ matrix (512 × 512 here), where i, j are integers with values 0,1,2,...,N - 1. It then follows that the potential for any point above the surface is given by

$$\phi(x,y,z) = \sum_{i=0}^{N-1} \sum_{j=0}^{N-1} \left\{ A_{i,j} cos\left[\frac{2\pi(ix+jy)}{L}\right] + B_{i,j} sin\left[\frac{2\pi(ix+jy)}{L}\right] \right\} e^{-k_z(i,j)z} \tag{5.5}$$

where $k_z(i,j) = \frac{2\pi}{L}\sqrt{i^2+j^2}$. Not all Fourier components were required to achieve an accurate reproduction of the surface potential. As can be seen from Eq. 5.5, high-frequency components would also have very short decay lengths along the Z axis. 50 nm was chosen as the lower limit since components with shorter periods would make only negligible contributions to the potential at the values of z of interest here. Also, with a $1\mu m$ wide area measured, it was sensible to neglect components with periods greater than 1 μm. It was determined that limiting the potential to only the 277 most prominent Fourier components within the allowed range produced no noticeable difference in the simulation, but greatly reduced the computational burden. The measured surface potential is presented in Figure 5.3 along with the $z = 0$

potential which was reconstructed using the 277 Fourier components and Eq. 5.5.

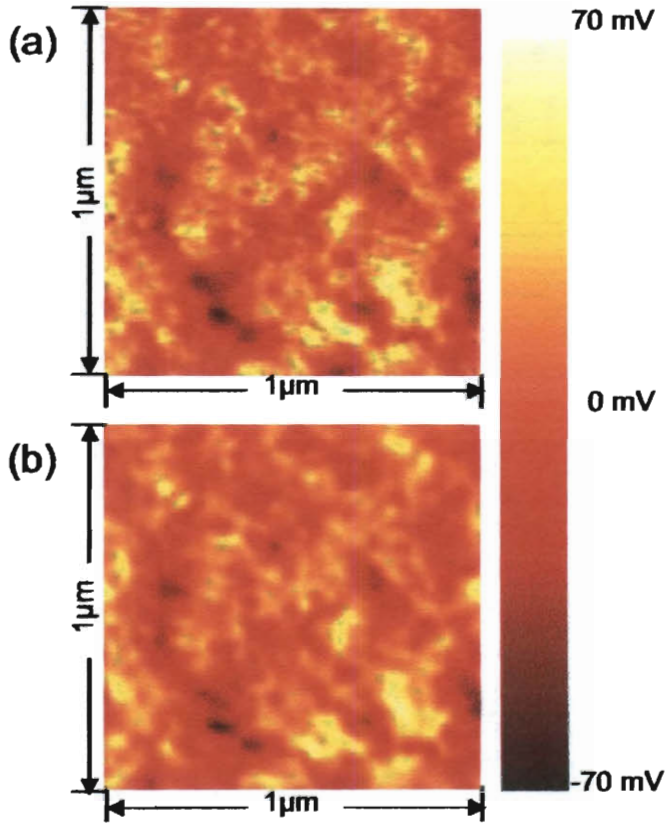

Figure 5.3 : (a) Measured surface potential. (b) z=0 potential based on the 277 most prominent Fourier components.

The reconstructed potential clearly reproduces the key features of the actual potential, but illustrates that the potential array has been band-pass filtered. It is assumed that the $1\mu m \times 1\mu m$ measured area adequately represents the surface potential as a whole. To justify this assumption, measurements were performed over $1\mu m \times 1\mu m$ areas of two different Au(111) samples. The two measurements were

extremely similar in feature size and amplitude. Although the two potential arrays showed different features, they resulted in indistinguishable simulations. Experimentally, the metastable xenon beam illuminates several square millimeters of the gold surface, which is sufficiently large to ensure that it is interacting with an "average" surface.

5.1.2 Determination of the Ionization Point

The impact locations are randomly distributed across the $1\mu m \times 1\mu m$ surface. Each point is traced backwards at the specified incident angle to define its trajectory. Each trajectory is searched to find the furthest point from the surface at which ionization would occur. This is accomplished using a binary search algorithm which tests the center point along the trajectory to determine if ionization occurs. Depending on the result, the critical distance for ionization will either be known to lie above or below that point, Thus halving the area being tested. Repeating the process progressively halves the range remaining until the bounds lie within some specified tolerance of one another.

It is possible that trajectories passing over changes in potential observe non-monotonic behavior in the height of the potential barrier for points along the trajectory. Figure 5.4 shows the height of the barrier vs. atom-surface separation for three random trajectories over the measured surface potential. While barrier height vs. distance from surface is monotonic for an ideal surface, Figure 5.4 shows it can

be non-monotonic when a "real" surface potential is considered.

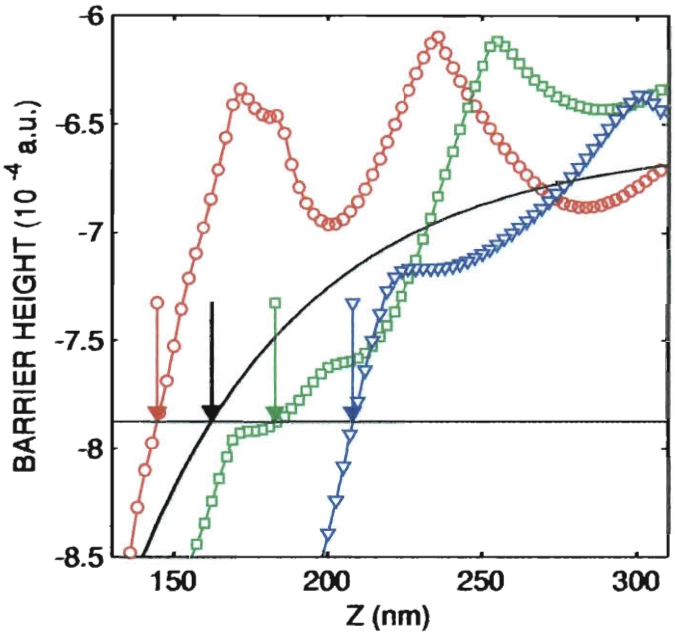

Figure 5.4 : Height of barrier vs. atom-surface separation for 3 random impact sites (o,□,△) and for an ideal surface (—) incident at 13° in an applied field of 550 $V \cdot cm^{-1}$. The horizontal dashed line indicates the binding energy of an n=26 Rydberg atom, and the arrows indicate the ionization distances.

Although a rare occurrence (~10% or less), such non-monotonic barrier heights can result in an "island" of ionization in which there are two ranges over which ionization would occur separated by a range in which ionization would not occur. This is problematic for a binary search since failure to ionize at a given point does not necessarily mean that ionization would not occur further from the surface. To remedy this, once an ionization distance is determined using a binary search, it is used to define a range of larger distances for a more in depth search. This range is

divided into several sections, each of which is searched independently to determine the maximum ionization distance for the trajectory.

To determine the barrier height at a given location, the potential is analyzed along various paths from the core to the surface as illustrated in Figure 5.5. It was determined that limiting these calculations to a 30° half-angle cone had no impact on the results of the simulation. The potential for each path resembles the total potential shown in Figure 5.1, and the electron potential is given by

$$\begin{aligned} V(x,y,z) &= \frac{-1}{\sqrt{\rho^2+(Z-z)^2}} - \left(\frac{1}{4z} - \frac{1}{4Z}\right) + \left[\frac{1}{\sqrt{\rho^2+(Z+z)^2}} - \frac{1}{2Z}\right] \\ &+ F(z-Z) - \phi(x,y,z) + \phi(X,Y,Z) \end{aligned} \tag{5.6}$$

where (x,y,z) is the electron position, (X,Y,Z) is the core position, F is the applied field, $\phi(x,y,z)$ is given by Eq. 5.5, and $\rho^2 = (x-X)^2 + (y-Y)^2$. The height of the barrier along each path is determined, and the lowest of these is assumed to be barrier height at a given location.

With a most-probable velocity of 450 $m \cdot s^{-1}$ and a typical surface potential feature size of a few hundred nanometers, the time which our atoms will spend over each feature is $\sim$1 ns. Since the orbital periods for the Rydberg atoms employed are on the order of $\sim$1 ps, it is assumed that the electron will undergo many orbits near a given location. Thus it is reasonable to assume that if any path from the core to the surface has a potential barrier less than the binding energy of the electron, then the electron will have a sufficient opportunity to find it and ionize. Once the barrier height is determined, it is compared to the binding energy of the Rydberg electron

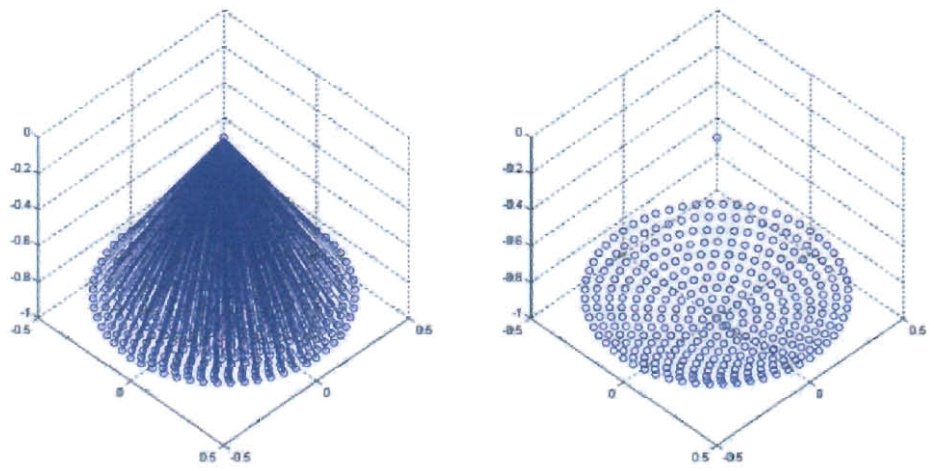

Figure 5.5 : Illustration of paths for which barrier height is computed within a 30° half-angle cone, and assuming a core-ion at (0,0,0).

do determine whether or not ionization would occur.

5.1.3 Binding Energy

The binding energy of the Rydberg atom's electron is assumed to be the Stark energy for the given applied field. With a field rise time of $\sim 1\ \mu s$, passage through the Stark manifold is assumed to be adiabatic. The energy is determined using hydrogenic Stark energies, which to second order are given by [19]

$$W = -\frac{1}{2n^2} + \frac{3}{2}n(n_1 - n_2)F - \frac{1}{16}n^4\left[17n^2 - 3(n_1 - n_2)^2 - 9m_\ell^2 + 19\right]F^2. \quad (5.7)$$

As mentioned in Section 2.1.2, n_1 and n_2 are constrained by Eq. 2.8. As described in Section 4.1, zero-field Xe(nf) Rydberg states correlate with the lowest lying states

in the neighboring Stark manifold of the same n. Figure 5.6, although calculated for sodium, provides a general example of how the energy of the lowest-lying state evolves in an adiabatically increasing electric field.

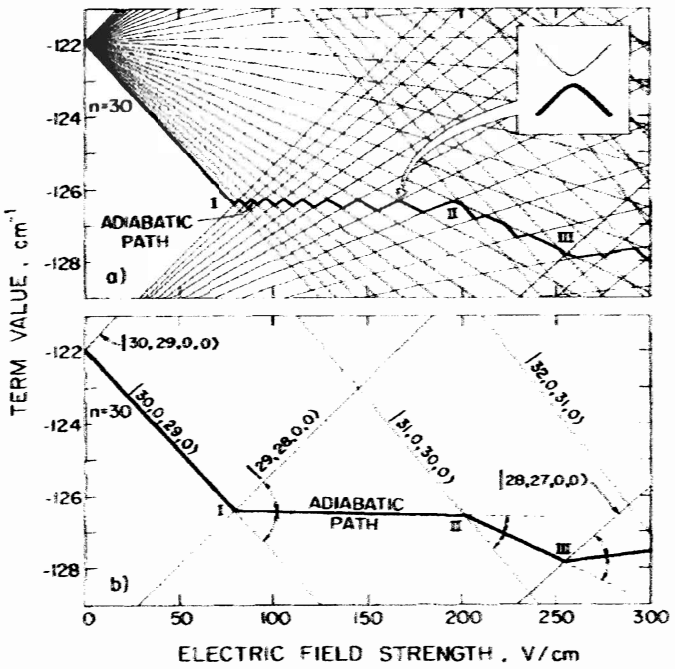

Figure 5.6 : (a) Schematic representation of adiabatic path for the lowest member of the $|m_\ell|$=0 Stark manifold for n=30 in Sodium. Inset shows an adiabatic crossing. (b) Simplified reconstruction described in text [56].

Initially, the energy of the state decreases with respect to the applied field until the point where the red-most state of the manifold for n crosses the blue-most state of the manifold for $n-1$ (labeled as "I" in the figure), known as the Inglis-Teller limit. The atom will then successively assume the character of the next red-most state, followed by the next blue-most state, and so on. In this regime, only small changes in energy

occur, and to a good approximation, the energy of the state can be considered to be constant. This assumption is valid until the path crosses the red-most state of the n+1 Stark manifold (labeled "II" in the figure). From this point, the energy can be approximated as the average between the energy of the n+1 red-most state, and the approximately constant value assumed between I and II. Although a fourth region is indicated in the figure, ionization typically occurs before it is reached in xenon.

The algorithm first determines the crossing points for a given value of n, then determines which region the given applied field lies within. The Stark energy for the given n can then be easily calculated using the appropriate equations for that region. These Stark energy calculations were used in conjunction with the over-the-barrier model to determine the expected critical fields for ionization. The predicted critical fields were found to be in excellent agreement with those determined experimentally (typically within $\sim 2\%$).

5.1.4 Ion Trajectory Calculation

With the ionization point determined, a velocity is randomly selected from the known distribution (Figure 4.12). The incident angle and magnitude of velocity allow for determination of the x and z components of velocity, v_x, and v_z, respectively (v_y is assumed to initially be zero). The values of x, y, and z are simply the coordinates of the ionization point. These six values specify the initial conditions for the equations

of motion for the ion which can be written (in atomic units) as

$$\begin{aligned} \ddot{x} &= \frac{1}{m}E_x(x,y,z) \\ \ddot{y} &= \frac{1}{m}E_y(x,y,z) \\ \ddot{z} &= \frac{1}{m}E_z(x,y,z) - \frac{\beta}{4mz^2} \end{aligned} \tag{5.8}$$

where m is the mass of the isotope (247,928 atomic units), E is the magnitude of the surface electric field along the specified axis, and $\beta = \frac{\epsilon-1}{\epsilon+1}$ is a factor based on the dielectric constant, ϵ, of the surface. For a metal surface such as those employed here, $\beta \simeq 1$. The electric field strength can be calculated simply by taking the gradient of the potential from Eq. 5.5.

Given the initial conditions, these equations of motion can easily be solved using a fourth-order Runge-Kutta algorithm. This algorithm numerically steps along the trajectory (using a step-size calculated to give errors below a defined tolerance) to determine the velocity, position, and time at each step. The trajectories are computed until either the ion impacts the surface, or reaches some specified distance from the surface (typically ~10,000 atomic units), beyond which image charge and surface fields are negligible whereupon the applied field dominates and collection is guaranteed.

5.1.5 Collection Efficiency Vs. Applied Field

This procedure of determining the ionization point, and tracking the resulting ion's trajectory to determine whether or not it is collected is repeated for many atoms. A minimum of several hundred trajectories are required at each applied field to obtain

statistically reliably results and determine the fraction of incident atoms that would be detected as ions within a statistical error $\lesssim 10\%$. Ideally, thousands of trajectories would be used ensuring even lower statistical error, however, considering the number points tested on each trajectory, the number of paths computed at each point, the number of individual points for which a potential is calculated along each path, and the number of Fourier components needed to compute a given potential, one can see how such a simulation can quickly become computationally intensive. A typical simulation, computing collection efficiencies at $\sim$10 different applied fields takes 1-2 *days* running 4 simultaneous threads on a quad-core CPU at 3.0 GHz. Such an algorithm does, however, lend itself to asyncronous parallel processing. So the algorithm could easily be adapted for use on a computing cluster in the future.

5.2 Data and Analysis

Field-dependent collection efficiencies determined at various incident angles for n=17, and n=20 on a Au(111) surface have been reported previously [1,3]. The laser modifications outlined in Section 3.3 increased the experimental capabilities, essentially allowing excitation of any n-level up to the continuum, although some features are observed (attributed to hyperfine structure) in the peak corresponding the excitation of $n \gtrsim 40$ for the ^{136}Xe isotope. Simulations have been conducted for the historical data, as well as for data spanning the new range of n-levels. Collection efficiencies were also measured for n=14, but will be presented in the next section.

Figure 5.9 shows the dependence of the measured collection efficiencies on applied field for n-levels ranging from n=17 to n=36 for incident angles of $\sim 5°$ and $\sim 14°$ as well as the corresponding simulations. The simulations however, were conducted at incident angles of 4° and 13°, which points a small systematic error in determining the incident angle. These incident angles represent the extremes possible with the current interaction region, and give components of velocity towards the surface which differ by a factor of ~3, thus changing the electric fields required to collect them by about an order of magnitude. The figure illustrates the impressive agreement between simulation and experiment over a wide range of n at both extreme angles, even though the applied fields required differ by more than order of magnitude.

5.3 n=14 Data and Analysis

The optical diode modifications described in Section 3.3.2 also allowed for excitation of Xe(14f) Rydberg atoms. The n=14 level has a zero-field life time of only ~2 μs, which is short relative to the timescale of the experiment. Because the longest lifetime measured in any applied field is on the order of the average flight time to the surface, radiative decay requires much more than a small correction.

Uncorrected collection efficiency data is presented in Figure 5.7. As anticipated, the collected fraction reaches, at most, $\sim 1/e$, but there is clearly structure present in the data. A comparison with Figure 2.6 shows that this structure corresponds to avoided crossings for the lowest state in the n=14 Stark manifold. A slight, but

reproducible dip is observed near 3 $kV \cdot cm^{-1}$ which likely corresponds to an avoided crossing with the Xe(16p) state. A much larger dip is observed near 5 $kV \cdot cm^{-1}$, which appears to coincide with the avoided crossing with the blue-most n=13 state. The effects of avoided crossings on n=14 collection efficiencies will be more obvious in Section 7.3.

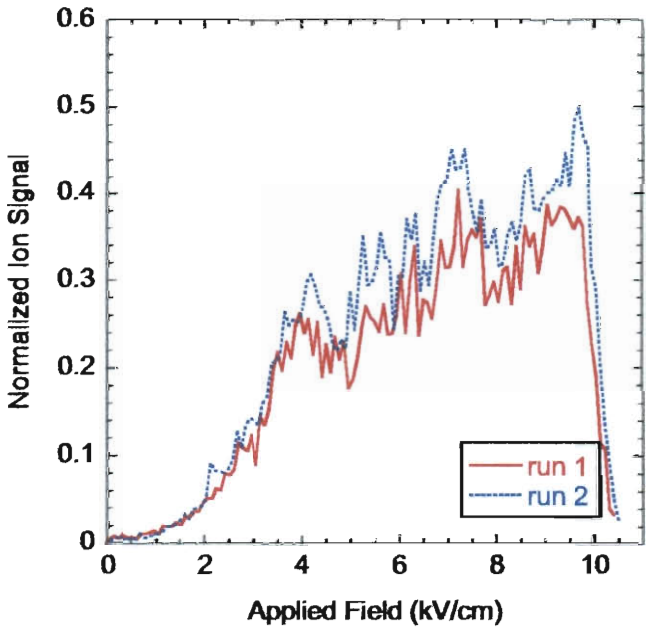

Figure 5.7 : (a) Uncorrected collection efficiency vs. applied field data for n=14 Rydberg atoms incident at 4.5°. Two data runs are presented with slightly different laser beam positions.

As described in Section 4.3, the radiative lifetime for n=14 was carefully measured at many applied fields. The measured lifetime was then used to correct the collection efficiency data, and the results are presented in Figure 5.8. The curve is essentially monotonic, just as observed for all higher n-levels.

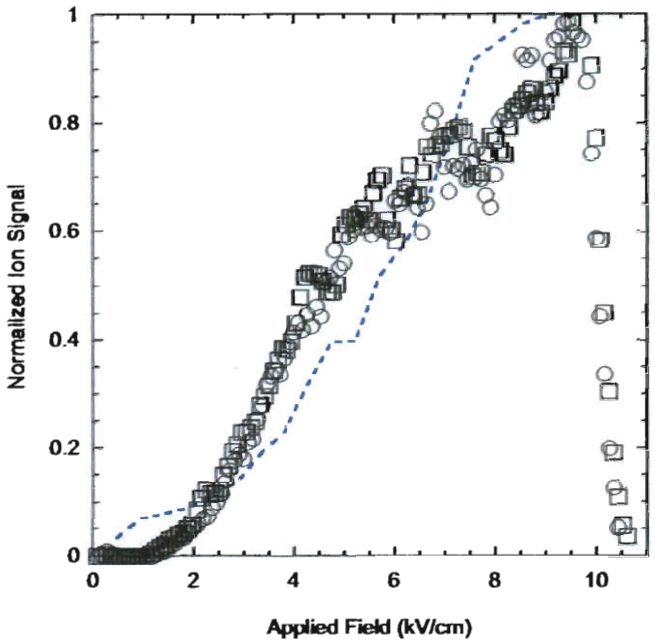

Figure 5.8 : Measured collection efficiency vs. applied field for n=14 atoms incident at 4.5° and corrected for radiative decay. Simulation results for the same conditions are also included (dashed line).

The fact that life time correction virtually eliminates the features associated with different spatial characteristics of the various Stark states is quite significant. It is clear from Figure 5.7 (and will be even more obvious in Chapter 7) that at least a significant fraction of atoms excited to the lowest n=14 Stark state are being transferred to other Stark states. The first major crossing, seen near 5 $kV \cdot cm^{-1}$ ($\sim$1 $\times$ 10^{-6} $a.u.$) in Figure 2.6 and Figure 5.7, corresponds to a transition to the highest n=13 state. As described in Section 2.1.2, this state will be oriented with the electron away from the surface. This configuration requires the core ion to be much closer to

the surface before surface fields and image charges can lower the barrier enough to cause ionization. Also, with the dipole inverted, strong applied fields should *raise* the barrier binding the electron to the core. Thus prime conditions for ionization would occur in a weak applied field over a negative region of surface potential. This negative potential however would certainly attract the resulting ions considering the applied field is weak. Thus, no ion collection is expected for largely blue-shifted states, yet the life time corrected collection efficiencies for red and blue states are indistinguishable.

This observation points to surface-induced mixing of a given Stark state. Such mixing may be due to the range of surface fields different Rydberg atoms experience prior to ionization, or possibly Stark-like avoided crossings [29–31] resulting from interactions with the atom's image charge field.

The n=14 simulation shown in Figure 5.8 does not illustrate quite the same level of agreement as the n levels presented thus far, but this is not unexpected. For an ideal surface, the over-the-barrier model predicts ionization to occur at atom-surface separations of $\sim 3.4n^2$ *a.u.*. n=14 would then be expected to ionize at an atom-surface separation of $\sim$35 *nm*. Thus the assumption that Fourier components with decay lengths less than 50 *nm* will not make a significant contribution to the potential is less valid for n=14 than for higher n levels. Although these high-frequency Fourier components have relatively small amplitudes, neglecting them causes a slight underestimation of the resulting potential and electric fields, which results in slightly less broadening of the simulation results than would be expected if higher frequency

terms were included.

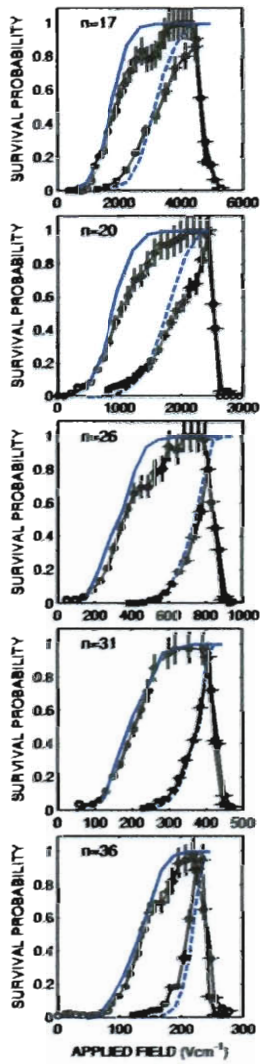

Figure 5.9 : Dependence of the normalized surface ion signals on applied field for several values of n. Measurements (o,□) made at angle of incidence of 5° and 14°, respectively are compared to simulations (—,- - -) for angles of incidence of 4° and 13° (see text).

Chapter 6

Rydberg Atoms as a Field Probe

The previous chapter illustrated the crucial role surface-electric (or "patch") fields play in Rydberg atom-surface interactions. It demonstrated that Monte Carlo techniques considering a known surface potential distribution along with a simple over-the-barrier model allow for excellent predictions of the dependence of surface-ion collection efficiency on the applied electric field. This chapter, however, will describe a novel technique for making quantitative determinations of an upper limit for patch field strength vs. distance from surface based on collection efficiency data.

6.1 Determining A First-Order Curve

For an ideal surface, conservation of energy dictates that the critical distance beyond which an atom must ionize in order to be collected is given by

$$Z_{crit} = \frac{T_\perp}{4F}\left[1+\sqrt{1+\frac{2\sqrt{F}}{T_\perp}}\right]^2 \tag{6.1}$$

where $T_\perp = \frac{1}{2}mv_\perp^2$ and F is the applied electric field strength. We also know from Eq. 5.1 that the ionization distance depends on the strength of the applied field. Thus increasing the applied field strength will allow collection from closer ionization distances, reducing Z_{crit}, and will also increase the over-the-barrier ionization distance,

Z_{OTB}.

It then stands to reason that at the surface-ion collection threshold, where the normalized signal first becomes nonzero, atoms are just beginning to ionize at Z_{crit}. The first atoms to be detected would naturally be the easiest ones to collect, or the atoms with the lowest velocities. Considering the velocity distribution presented in Figure 4.12, the lowest significant velocity is $\sim 350\ m \cdot s^{-1}$.

Thus it is expected that if Z_{crit} and Z_{OTB} are calculated assuming a velocity of $350\ m \cdot s^{-1}$, and an applied field equal to the experimentally determined threshold for surface-ion collection, the two should be equal. However, using n=20 as an example we see that this is not the case. The threshold for surface-ion collection of n=20 Rydberg atoms is $\sim 450\ V \cdot cm^{-1}$ which, assuming an incident angle of 4.5°, gives $Z_{crit} \cong 1800\ a.u.$, wheras $Z_{OTB} \cong 1430\ a.u.$. So for an ideal surface, $450\ V \cdot cm^{-1}$ would be insufficient to collect the slowest atoms.

A zeroth-order approximation of patch field strength was made by assuming that the applied field, F, was the sum of the threshold field, F_T and a uniform surface field, F_{surf}. Since the change in both Z_{crit} and Z_{OTB} is monotonic with respect to a change in F, and hence a change in F_{surf}, a search algorithm was employed to iterate F_{surf} to find the value which sets $Z_{crit} = Z_{OTB}$. This computation was conducted for the thresholds for the different n-levels at a 5° incident angle.

Figure 6.1 shows the values of average surface fields required plotted from the barrier location to the core location at the point of ionization. It is apparent that

the dependence of the surface field strength with distance from surface might be approximated as the sum of several exponential components, or even a power law. It is thus assumed that the stray surface field decreases approximately exponentially, at least over a small range of distances.

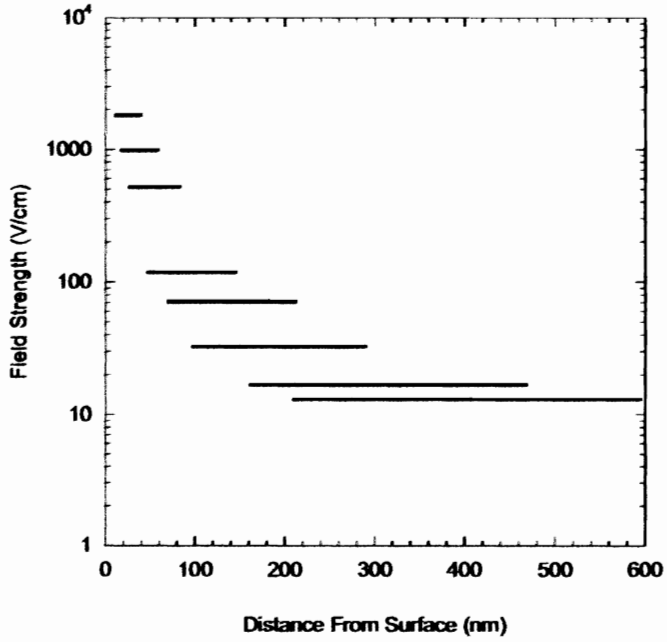

Figure 6.1 : Average surface fields required to give correct threshold field for surface-ion collection plotted from barrier-to-core at the ionization point for thresholds from 5° data for n=14, 17, 20, 26, 31, 36, 45, and 50.

The assumption of a surface field which decays exponentially from the barrier to the core allows for determination of a first-order curve. If the surface field strength is an exponential with respect to z, then the potential due to the surface fields (i.e.

the integral) is also exponential. The potential is assumed to have the form

$$V_{surf} = V_0 e^{-\frac{z}{Z_{dec}}} \tag{6.2}$$

where V_0 is the value of the potential at $z = 0$ and Z_{dec} is the decay length. This gives two degrees of freedom to the surface-potential, and consequently, there are many possible V_{surf} curves for each threshold which would set $Z_{crit} = Z_{OTB}$. For calculation of Z_{crit}, it is assumed that the field, F, is the sum of the applied field and the value of the surface field at ionization, or $V_{surf}(Z_{OTB})$. Several values of decay length were chosen manually, and the corresponding values of V_0 were determined using the search algorithm. The resulting potential curves are shown in Figure 6.2, again plotted from barrier-to-core at the ionization point. Decay lengths used range from 200 to 6400 a.u., incremented by factors of two.

Each V_{surf} curve is in a sense correct, as each would in fact yield a threshold for surface-ion collection which is identical to that which was determined experimentally. Truthfully, each curve is a slight underestimation due to the fact that field which turns the atom was approximated as the field at the ionization point. In reality the field strength will increase as the atom approaches the surface, thus helping turn the atoms and decreasing the value of Z_{crit} slightly. Nonetheless, each curve presents a plausible piece of the total potential curve due the surface potential variations.

Noting that a numerical value of potential is always relative to an arbitrary reference potential, it is clear that these potential curves can be translated vertically without modifying the change in potential from the core to the barrier or the field

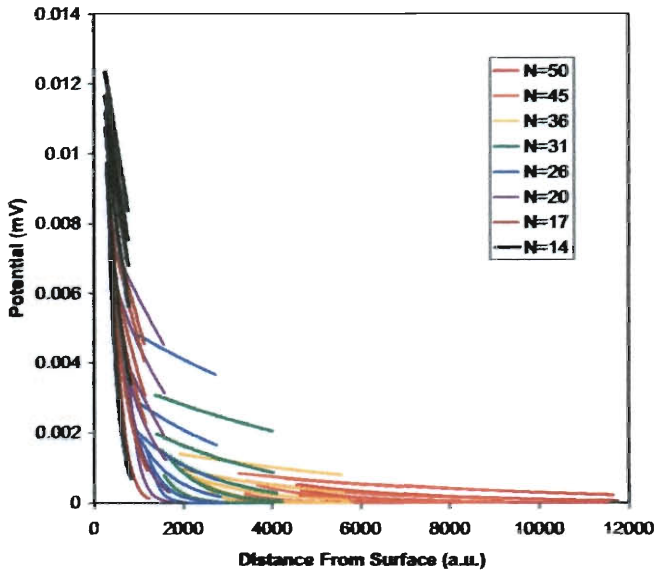

Figure 6.2 : Various surface potential curves which would give the experimentally determined thresholds for the given n-level.

strength. Thus an offset value can be added without impacting the ionization or collection conditions. Exploiting the fact that the potential and its derivative (the electric field strength) must be continuous, and noting that the potential curves for each n-level overlap slightly, it is possible to align certain V_{surf} curves to minimize errors at the crossings. This results in one continuous curve which would predict the experimentally determined thresholds for all n-levels. Fine-tuning some of the choices for Z_{dec}, and computing corresponding the values of V_0 can further improve the crossings. The resulting potential curve is shown in Figure 6.3, and represents what can be called a first order surface potential.

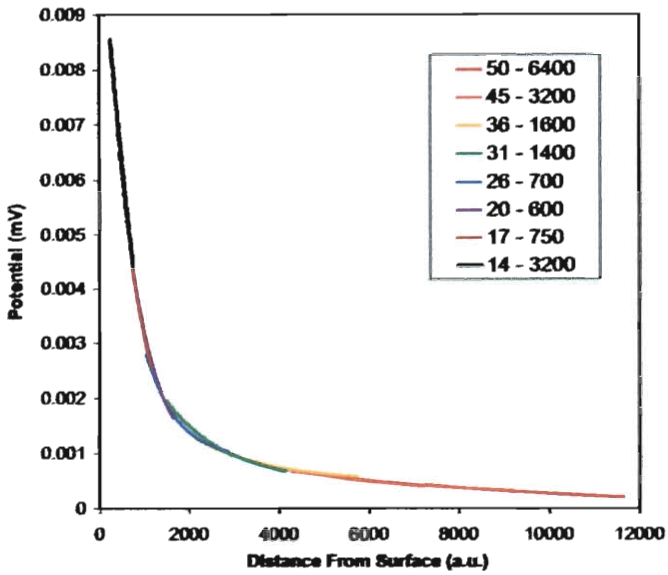

Figure 6.3 : Adjusted surface potential curves showing a continuous, first-order potential curve. The legend indicates "n-level - decay length".

6.2 Fine Tuning The Electric Field

The potential shown in Figure 6.3 is nicely fit with a sum of three exponentials:

$$V_{surf} = \sum_{i=1}^{3} A_i e^{-\frac{z}{Z_i}} \tag{6.3}$$

Determining the corresponding field strength is as simple as taking the derivative. However, this electric field would decay along the Z-axis, so in order to be physically reasonable, there must be some divergence in X and Y. This section will present an algorithm which accounts for the divergence and determines the error between the predicted and measured thresholds as a function of the surface-field parameters. Thus fine-tuning the surface-field parameters allows for the minimization of a sum-of-

squares error to determine the surface-field curve which best predicts all experimental thresholds.

6.2.1 Effective Z_{crit}

The approach presented in the previous section used Eq 6.1 with an approximation that F was equal to the measured threshold for surface-ion collection plus the surface field strength at the over-the-barrier ionization distance. In order to eliminate the need for such an approximation, Eq 6.1 can no longer be used. Furthermore, the exponentially decaying field alone is not physically realistic. In order to satisfy Laplace's equation, a divergence must be introduced. It is therefore assumed that the strength of the surface electric field which the ion will experience can be written as

$$E(X,Y,Z) = \sum_{i=1}^{3} E_i e^{-\frac{Z}{Z_i}} cos\left(\frac{X}{\sqrt{2}Z_i}\right) cos\left(\frac{Y}{\sqrt{2}Z_i}\right) \tag{6.4}$$

which now satisfies Laplace's equation. The ion collection threshold corresponds to the situation where the slowest atoms which ionize the furthest from the surface, i.e. where the stray field is at its maximum directed away from the surface, are just able to be collected. In other words, the threshold field is where the slowest atoms ionizing over the most positive surface potentials are just collected. For an electric field given by Eq. 6.4, the maximum positive surface potential occurs at X=0 and Y=0. Thus atoms considered for these calculations are assumed to ionize at X=0, Y=0.

Since the surface field effects ion-collection, and since Eq. 6.4 depends on X and Y, ion trajectories must be considered in the place of Z_{crit}. The trajectory of an

ion can be traced from the coordinate (0,0,Z) to determine whether or not an atom ionizing at the distance, Z, is collected. It is assumed that motion will be in the X-Z plane for the entire trajectory. A range of Z can be searched to determine the critical distance above which atoms are collected and below which they are lost. The critical distance is the effective Z_{crit}.

6.2.2 Minimizing Error

With a technique established for determining the effective Z_{crit}, a range of applied fields can be searched to find which field would set Z_{OTB} equal to the effective Z_{crit}. This value of applied field is the value for which the slowest atoms ($\sim$350 $M \cdot s^{-1}$) should ionize just far enough from the surface to ensure collection in the specified applied field. In other words, given values for the six constants needed to determine the potential in Eq. 6.3 (note: Eq: 6.4 simplifies to Eq. 6.3 at X=0, Y=0), the predicted threshold for ion collection can be determined.

The predicted thresholds were calculated for 14 experimentally observed thresholds, eight of which were determined at an incident angle of 4.5°, and six at 14°. The experimentally observed thresholds for surface ion collection are shown in Figure 6.4. The difference between an observed threshold and a predicted threshold was squared, and the squares summed over all 14 data sets. The surface potential parameters were systematically modified, just as if performing a curve-fit, to achieve as low a sum-of-squares as possible.

The gradient was taken to determine the surface field strength vs. distance from surface. Based on Eq. 6.3, The surface electric field strength will have the form

$$E_{surf} = \sum_{i=1}^{3} E_i e^{-\frac{z}{Z_i}}. \tag{6.5}$$

The values obtained from the error minimization routine are: $E_1 = 6.6\ kV \cdot cm^{-1}$, $Z_1 = 22\ a.u.$, $E_2 = 5.4\ kV \cdot cm^{-1}$, $Z_2 = 740\ a.u.$, $E_3 = 380\ V \cdot cm^{-1}$, and $Z_3 = 2900\ a.u.$. For comparison, the RMS value of the field strengths obtained from the gradient of Eq. 5.5 were computed. Both surface field strength curves are shown in Figure 6.5.

The surface field strength determined from the thresholds is clearly larger than the RMS of the measured potential for a Au(111) surface. This is not unexpected since, as stated earlier, the thresholds correspond to the slowest atoms ionizing over the most positive surface potentials. This is precisely why the field strengths derived from the experimentally observed thresholds correspond to an upper-limit of the distribution of field strengths which will be present on a real surface.

The surface fields obtained from the experimental thresholds were used in conjunction with the Monte Carlo model in order to determine the thresholds predicted by simulation. Figure 6.6 shows the outstanding agreement between the predicted thresholds and those observed experimentally.

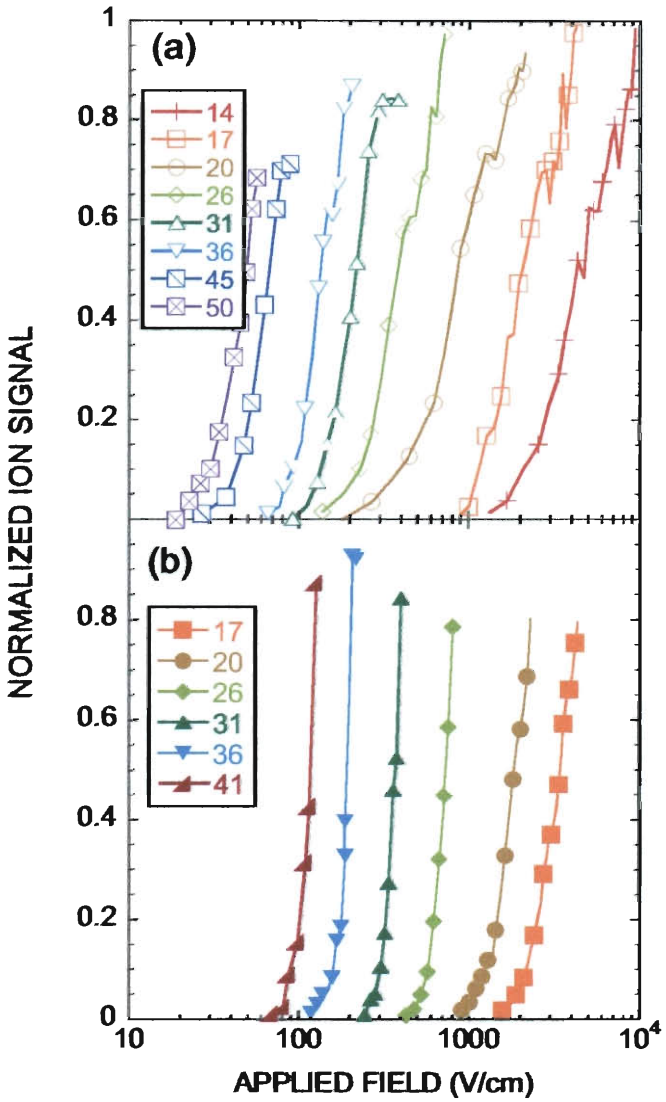

Figure 6.4 : Experimentally observed thresholds for surface-ion collection for Ryberg atoms of the specified n-level incident at 5° (a), and 14° (b) on a Au(111) surface.

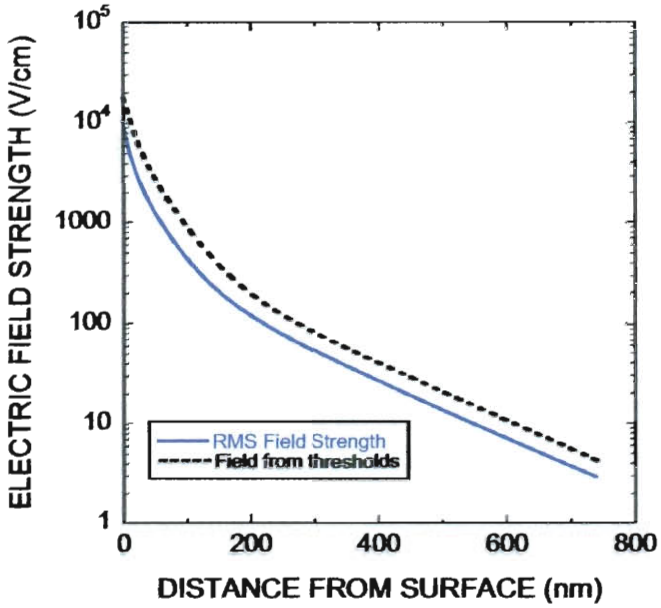

Figure 6.5 : Surface electric field strength vs. distance from surface determined from experimentally observed thresholds for ion collection together with RMS values of field strength derived from measured variations in surface potential.

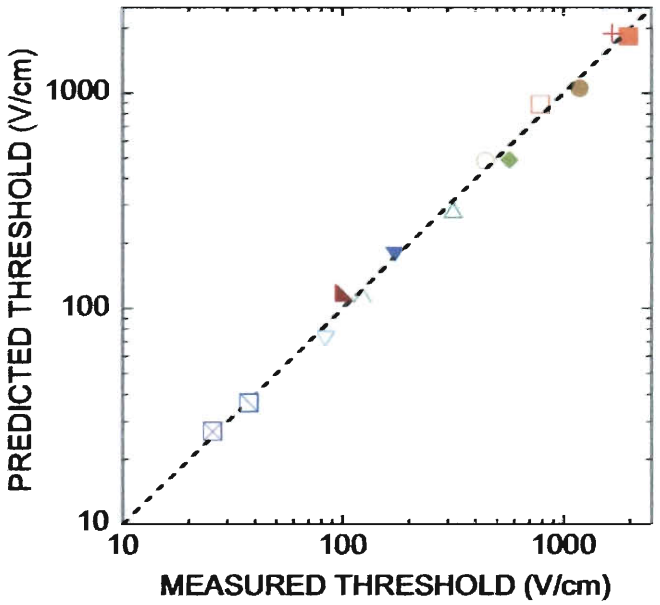

Figure 6.6 : Predicted threshold fields or ion-collection vs. observed threshold fields. Symbols used correspond to the various n-levels and angles in Figure 6.4.

Chapter 7

Progress Towards Control of Surface Fields

The 2-D Monte Carlo model mentioned in Chapter 5 suggested that a surface patterned with an array of long, parallel wires could be used to radically control and enhance ion collection efficiencies in a given applied field. Simulations showed that using applied fields on the order of $\sim 10\ kV \cdot cm^{-1}$ (essentially the current experimental limit), ions resulting from surface ionization of Rydberg atoms with values of n as low as $n \sim 10$ could be collected with near unit efficiency using a surface comprising an array of periodic 1 μm wide wires, with 1 μm spacing, alternatingly biased at $\pm$ 1 V. n=10 Rydberg atoms field-ionize at $\sim$ 75 $kV \cdot cm^{-1}$, which is difficult to achieve with mirror-polished parallel plates, let alone with a wire-mesh which would permit ions to pass through and be detected. Thus a patterned array of wires promises efficient detection of low-n atoms which can not be detected via direct field ionization.

7.1 Simulations of Collection Enhancement

The enhancement in ion collection efficiencies that can be achieved using a patterned wire array is most drastic at lower n-levels. Simulations for n=14 Rydberg atoms are presented for the special cases where the incoming atoms are incident perpendicular to the wires, Figure 7.1, and parallel to the wires, Figure 7.2. These two figures

demonstrate two very different behaviors.

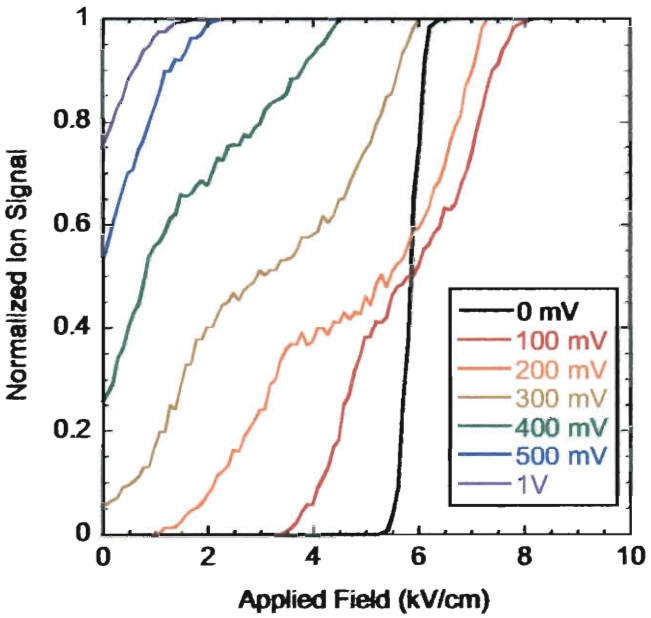

Figure 7.1 : Simulated collection efficiencies for n=14 Rydberg atoms incident perpendicular to a periodic array of 1 μm wide wires, with 1 μm spacing that are alternatingly biased at $\pm$ the indicated voltages at a 4° incident angle.

For atoms incident perpendicular to the wires, it is clear that increasing the wire bias significantly increases collection efficiency. For large wire biases however, a further increase in bias results in little change in collection efficiency. For the case of atoms incident parallel to the wires, those atoms whose incident trajectories travel along negative features must get very close to the wire surface before ionization can occur, resulting in a low probability of collection, whereas atoms over whose incident trajectories travel along positive wires ionize far from the surface, and are likely to be collected. This results in an ion collection efficiency that is close to 50% for large

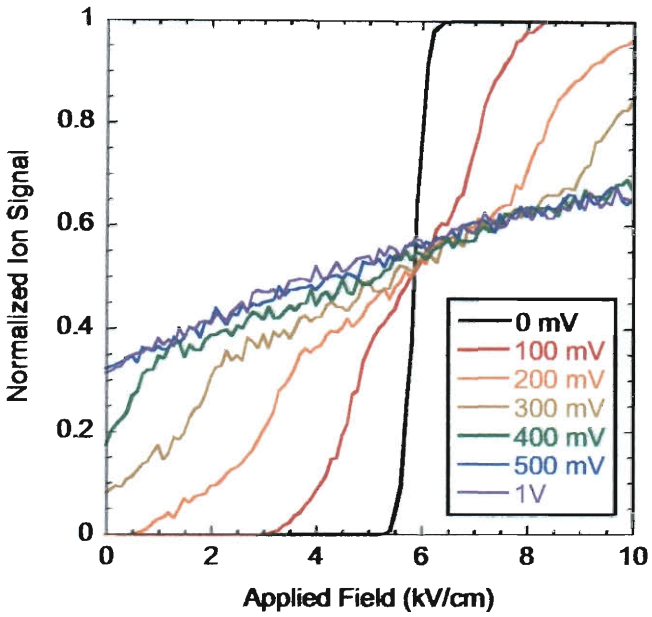

Figure 7.2 : Simulated collection efficiencies for n=14 Rydberg atoms incident parallel to a periodic array of 1 μm wide wires, with 1 μm spacing that are alternatingly biased at $\pm$ the indicated voltages at a 4° incident angle.

wire biases, and is essentially independent of the applied ion collection field.

Similar results have been observed in simulations at n=17, n=20, n=26 and n=31, although the wire bias beyond which the collection efficiency is little changed reduces with increasing n. For example, the saturation bias for n=20 is $\sim \pm 250\ mV$, whereas for n=14, the saturation bias is $\sim \pm 500\ mV$.

7.2 Sample Fabrication

To test the above predictions, a sample was designed comprised of two interleaved comb-shaped electrodes, with the wires alternatingly connecting to one of two main

electrodes. Considering the width of the metastable xenon beam and the large change in impact position which results from a small change in incident angle, it was determined that the minimum width of a usable sample must be 8 *mm*. Since it was desirable to construct a sample which could be rotated 90° to demonstrate the effects of varying the azimuthal angle of incidence, the sample had to be a square, a minimum of 8 *mm* on a side.

Patterning one micron features is just beyond the capabilities of the photo-lithography equipment available at Rice. While E-beam lithography can provide the required resolution, the capabilities of tools available at Rice could not extend to the required area. Commercial photo lithography was also not a possibility, since the anti-reflective coatings employed are strong dielectrics which would need to be removed via mechanical polishing, which would introduce particulates, solvents, and a whole host of possible contaminants. The polishing process would also leave a surface finish far inferior to that of an evaporated or sputter-deposited surface.

Instead, a lab at UT Austin which is part of the national nanotechnology infrastructure network (NNIN) was utilized as it possesses an EBL writer capable of patterning 8" wafers. Several materials were considered for both the wires and the substrate. Noble metals such as gold and platinum were preferred since their lack of an oxide layer minimizes the potential for surface charging. In order to compare to simulations, preservation of the 1:1 ratio of width-to-spacing is also an important consideration. With a film thickness which is not negligible relative to the feature

size, undercutting of the resist associated with a chemical (or "wet") etch would be problematic. Thus a more directional etching option is required. Reactive ion etching (RIE), also known as plasma or "dry" etching, is the industry standard solution to this problem. However, dry etches for gold and platinum are extremely problematic, as they tend to etch everything, including resist material and substrates.

Lift-off techniques are also a poor choice here. Since E-beam lithography is employed, a conductive substrate is required to sink the current of the electron beam. Thus patterning resist material on a blank insulating wafer is not possible. Furthermore, with the entire sample face being comprised of 1 μm wide gaps, the likelihood of some of the removed metal lodging between two wires and causing shorts is quite high. In fact, such shorts were observed all over the surface of a 3 μm gold wire sample which was fabricated as a test using photo-lithography and a lift-off technique.

Chromium was selected as the metal of choice for wire fabrication because although it oxidizes, its oxide layer is self-limiting. Evaporating 20 nm of chromium onto a Au(111) substrate had no noticeable impact on the measured collection efficiencies. Thus it was assumed that fields above a chromium surface were no worse than those above gold. This was later confirmed via measurements of a 60 nm chromium film evaporated on a quartz substrate. The experimental data, taken at a 4° angle of incidence at n=20 were indistinguishable from those of a Au(111) surface.

Since chromium is in fact a reactive material, it can easily be dry etched. RIE attempts to remove a given material selectively by forming a volatile compound. In

the case of chromium, $CrCl_2O_2$ is the ideal choice. $CrCl_2O_2$ has a vapor pressure of 1 $mm\ Hg$ at a temperature of -18.4 °C [57], which makes it ideal for RIE.

It was determined that sapphire (Al_2O_3) would be the ideal substrate, although quartz was chosen due its significantly lower cost. A 60 nm chromium film was deposited using E-beam evaporation. The Cr-on-quartz wafers were taken to the NNIN node at UT Austin, and a 350 nm coating of ZEP520A resist material was applied. Each wafer was loaded into the EBL writer, and patterned over the course of a 12-hour exposure. The patterns were developed, and the wafers were brought back to Rice.

The RIE process used was developed specifically for this project. It was determined that 10 SCCM O_2, and 60 SCCM Cl_2 at a pressure of 50 mT, with an RIE power of 100 $Watts$ and an inertially confined plasma (ICP) power of 350 $Watts$ gave a Cr etch rate of about 70 nm per minute. This etch process utilized excess amounts of Cl_2 intentionally to aid in the removal of chromium oxides which typically must be removed via argon-sputtering before Cr etching is possible. The selectivity between Cr and the resist was sufficient to allow etching of 60 nm of Cr, but the numerical value of the selectivity was never determined. The process lead to dramatic heating of the sample, and after every 30 seconds in the plasma the chamber was brought up to atmospheric pressure with dry-nitrogen to allow the sample to cool. This prevented the resist material from melting. Future attempts should utilize RIE equipment at UT Austin, as the equipment there employs helium back-cooling to eliminate this

7.3 Experimental Observations

Surface ion collection efficiencies at the patterned wire surface with no biases applied were observed to be substantially higher than those for a Au(111) surface at low applied fields, pointing to stronger surface fields likely due to exposed insulators. As discussed in Section 7.1, the wire bias needed to saturate the increase in collection efficiency is higher at lower n-levels. Thus n=14 was selected for this investigation in order to minimize sensitivity to "biases" related to charging of the exposed insulator. The data for n=14 Rydberg atoms incident perpendicular to the wires are shown in Figure 7.4. The higher collection efficiencies associated with the wire surface accentuate the structure seen in Figure 5.7 and described in Section 5.3. The same data are presented after correcting for radiative decay in Figure 7.5. As with the Au(111) surface, the features attributed to avoided crossings in the Stark manifold are essentially eliminated after correcting for radiative decay.

Unfortunately, even though the resistance between the two arrays of wires on the patterned surface was a few hundred $k\Omega$, applying a bias to the wires as large as ± 2 V had no effect on the data. It was determined that the surface resistivity of quartz can be reduced by up to eight orders of magnitude in a humid environment [58]. Calculations showed that the surface conductivity of the quartz substrate might be sufficient to permit a leakage resistance between the tip of a wire and the neighboring electrodes which is less than the resistance along a wire. Basically, the biased surface was acting more like a potential gradient than a periodic variation between positive

factor. Lastly, the resistance between the electrodes was observed to drop by at least a factor of four immediately when the ion collection field was applied. While this field is constant on the timescale of the experiment, it is pulsed on and off at $\sim 3\ kHz$. This may point to some piezoelectric effects within the quartz substrate.

All issues above are related to the choice in material. A sapphire substrate will offer substantially higher surface and bulk resistivities, and should not exhibit any piezoelectric effects. A more conductive metal and a thicker film will reduce the resistance of the wires. Some experimentation with removal of the resist should allow for minimizing the amount of material remaining, possibly using an ultrasonic cleaner. All of these factors should allow for the fabrication of a functional patterned wire surface.

Chapter 8

Conclusions and Future Directions

This work has documented significant advances in both the experimental apparatus used to study Rydberg atom-surface interaction and the theory used to interpret the experimental data. The laser modifications have increased the number of n-levels possible for study from two, to $\sim$25. Long-wavelength instabilities that had plagued the laser system have been all but eliminated.

It has been shown that evaporated Au(111) surfaces are far from equipotential surfaces. Several possible explanations could account for these surface potentials, including potential differences associated with different crystallographic orientations of the grains in the film, potentials due to impurities or adsorbates, or possibly even something deposited on the surface by the xenon beam. However, if the surface potential is measured the effects of stray fields can be taken into account with the aid of a Monte Carlo model. This model provides results that are in excellent agreement with the experimental data.

Not only was a measured surface potential used to explain experimental data, but the data were used to make quantitative estimates of the maximum patch field strength vs. distance from surface. Using a three component exponential decay excellent agreement between the measured and predicted thresholds was observed for

a broad range of n and angle of incidence. Also, the decay characteristics of the stray fields are in good agreement with the RMS fields derived from the Fourier components of the measured surface potential. The present approach to measurement of stray surface patch fields represents one of the first practical applications for Rydberg atoms to date.

Simulations demonstrate that by carefully engineering local surface fields the ion collection efficiency can be greatly increased. Such an increase can yield extremely efficient detectors for low-n Rydberg atoms, which otherwise would require fields of $\gtrsim 100\ kV \cdot cm^{-1}$ for direct field ionization, that exceed the breakdown limit even for polished and conditioned parallel plate electrodes. Significant progress has been made towards constructing a patterned electrode surface for controlling local surface fields.

Although the Cr-on-quartz wires were unsuccessful, future attempts will no doubt prove to be successful. Replacing the quartz substrate with sapphire will eliminate the surface conductivity issues associated with humidity. Sapphire's bulk resistivity is also superior to that of quartz by $\sim$4 orders of magnitude. Cr is also a fairly resistive metal, and swapping it for one of the noble metals could decrease wire resistances by $\sim$2 orders of magnitude. With time and effort, it will be possible to develop a dry etch process for either gold or platinum. In fact, it was determined that Pt could be etched in a mixture of Ar, CF_4, and Cl_2 [61]. This process, however, consumes the resist material quickly. A Silicon nitride hard-mask was considered as a possible solution but it was determined that selectivities between Pt and SiN_x would be at

best 1:1, indicating that a thick nitride layer would be required. If care is taken to tailor the process to ensure that it gives a low anisotropy (or highly directional) etch, the Pt process can theoretically be made to work. The Pt process would also etch exposed sapphire, so the sapphire etching would also need to be highly directional in order to ensure that undercutting does not remove the sapphire which supports the wires.

The avoided crossings also provide unique opportunities for future experiments. It was observed that atoms in various Stark states ionize at similar atom-surface separations due to surface induced mixing. If however the surface was a true equipotential, then all atoms would experience identical conditions as they approach the surface. This might allow for direct testing of theoretical predictions. Several approaches might be employed to finding a true equipotential surface. If the surface potentials are due to grain structure or oxides, then they can be eliminated using a surface of highly-oriented pyrolitic graphite (HOPG). HOPG is comprised of many layers of graphene that have been annealed under tremendous pressure at temperatures of $\sim$3000 $^{\circ}K$. Individual grains can be over a centimeter across, and typical grains are several mm. Such a surface would have very few crystalline defects in the area illuminated by the atom beam.

The fact that a Au(111) surface and a Cr-on-quartz surface show identical surface fields may point to an impurity deposited on the surface by the metastable beam itself. In this case, a liquid metal surface may help keep such impurities from building up

on the surface by allowing them to flow into the bulk. Several Indium-Gallium alloys are available with melting points of $\sim$10 $^{\circ}C$. Indium and Gallium posses the largest liquid range of any metal, with a boiling point well beyond 1000 $^{\circ}C$. It is then no surprise that these alloys have extremely low vapor pressures, making them a much better choice than mercury. The alloys wet everything from glass, to silicon, to gold, to nickel, etc.

In summary, this work has shown that when the stray fields on surfaces are taken into consideration, the ionization of Rydberg atoms near a surface is well-described by a simple over-the-barrier model. Furthermore, the effects of the stray fields on the experimental data can be exploited to make quantitative estimations of the maximum strength of the stray fields on a given surface. It has also shown that control of stray fields can be used to enhance Rydberg atom detection, including low-n Rydberg atoms that are impossible to directly field-ionize. This work suggests several possible avenues for future research, including studying Rydberg atom interaction with more "ideal" surfaces and studying fields on micro and nano structured surfaces. With miniaturization being the driving force behind the electronics and data storage industries, surface properties are becoming increasingly important relative that of the bulk. Thus a novel approach for characterizing fields on surfaces may prove to be an extremely valuable tool in the years to come.

Bibliography

[1] D. D. Neufeld, H. R. Dunham, S. Wethekam, J. C. Lancaster, and F. B. Dunning *Surf. Sci.*, vol. 602, p. 1306, 2008.

[2] D. D. Neufeld, H. R. Dunham, S. Wethekam, J. C. Lancaster, and F. B. Dunning *Phys. Rev. B*, vol. 78, p. 115423, 2008.

[3] H. Dunham, *Angular Dependence of Xenon Rydberg Atom Ionization at Conducting and Semiconducting Surfaces.* PhD thesis, Rice University, Department of Physics and Astronomy, 2007.

[4] C. I. Sukenik, M. G. Boshier, D. Cho, V. Sandoghdar, and E. A. Hinds *Phys. Rev. Lett.*, vol. 70, p. 560, 1993.

[5] B. C. Stipe, H. J. Mamin, T. D. Stowe, T. W. Kenny, and D. Rugar *Phys. Rev. Lett.*, vol. 87, p. 096801, 2001.

[6] S. Kuehn, R. F. Loring, and J. A. Marohn *Phys. Rev. Lett.*, vol. 96, p. 156103, 2006.

[7] J. M. Obrecht, R. J. Wild, and E. A. Cornell *Phys. Rev. A*, vol. 75, p. 062903, 2007.

[8] J. Labaziewiez, Y. Ge, D. R. Leibrandt, S. X. Wang, R. Shewmon, and I. L. Chuang *Phys. Rev. Lett.*, vol. 101, p. 180602, 2008.

[9] T. F. Gallagher, *Rydberg Atoms.* Cambridge: Cambridge University Press, 1994.

[10] S. E. Kupriyanov and L. Y. Karpov *JETP Lett*, vol. 5, p. 197, 1967.

[11] C. Fabre, M. Gross, and J. M. R. *et al*, *J. Phys. B*, vol. 16, p. L671, 1983.

[12] G. E. McCown, C. R. Taylor, and C. A. Kocher *Phys. Rev. A*, vol. 38, p. 3918, 1988.

[13] D. F. Gray, Z. Zheng, and K. A. Smith *Phys. Rev. A*, vol. 38, p. 1601, 1988.

[14] W. F. Edgell, *Argon, Helium, and the Rare Gasses.* ed. G. A. Cook, New York: Interscience Publishers, 1961.

[15] H. Hotop, *Atomic, Molecular, and Optical Physics.* eds. F. B. Dunning and R. G. Hulet, San Diego: Academic Press, 1996.

[16] R. F. Stebbings, C. J. Latimer, W. P. West, F. B. Dunning, and T. B. Cook *Phys. Rev. A*, vol. 12, p. 1453, 1975.

[17] R. D. Knight and L. Wang *J. Opt. Soc. Am. B*, vol. 2, p. 1084, 1985.

[18] C. Haich, "Design and development of an apparatus to study atom-surface interactions using rydberg atoms," Master's thesis, Rice University, Department of Physics and Astronomy, 1999.

[19] D. Kleppner, M. G. Littman, and M. L. Zimmerman, *Rydberg States of Atoms and Molecules.* eds. R. F. Stebbings and F. B. Dunning, Cambridge: Cambridge University Press, 1983.

[20] C. Oubre, P. Nordlander, and F. B. Dunning *J. Phys. Chem. B*, vol. 106, p. 8338, 2002.

[21] J. N. Bardsly *Case Studies Atomic Phys.*, vol. 4, p. 299, 1974.

[22] G. D. Mahan and K. R. Subbaswamy, *Local Density Theory of Polarizability.* New York: Plenum Press, 1990.

[23] A. L'Huillier, L. A. Lompré, D. Normand, J. Morellec, M. Ferray, J. Lavancier, G. Mainfre, and C. Manus *J. Opt. Soc. Am. B*, vol. 6, p. 1644, 1989.

[24] L. Wang and R. D. Knight *Phys. Rev. A*, vol. 34, p. 3902, 1986.

[25] P. Nordlander and J. C. Tully *Phys. Rev. Lett.*, vol. 61, p. 990, 1988.

[26] F. B. Dunning, H. R. Dunham, C. Oubre, and P. Nordlander *Nucl. Inst. Meth. Phys. B*, vol. 203, p. 69, 2003.

[27] A. V. Chaplik *Sov. Phys. JETP*, vol. 27, p. 178, 1968.

[28] U. Wille *Phys. Rev. B*, vol. 50, p. 1888, 1994.

[29] P. Nordlander *Phys. Rev. B*, vol. 53, p. 4125, 1996.

[30] P. Nordlander and F. B. Dunning *Phys. Rev. B*, vol. 50, p. 8083, 1996.

[31] P. Nordlander and F. B. Dunning *Nucl. Inst. Meth. Phys. Res. B*, vol. 125, p. 300, 1997.

[32] P. K. ürpick, U. Thumm, and U. Wille *Phys. Rev. A*, vol. 57, p. 1920, 1998.

[33] N. N. Nedeljković and L. D. Nedeljković *Phys. Rev. A*, vol. 72, p. 032901, 2005.

[34] F. B. Dunning, S. Wethekam, H. R. Dunham, and J. C. Lancaster *Nucl. Inst. Meth. Phys. Res. B*, vol. 258, p. 61, 2007.

[35] S. Wethekam, H. R. Dunham, J. C. Lancaster, and F. B. Dunning *Phys. Rev. A*, vol. 73, p. 032903, 2006.

[36] H. R. Dunham, S. Wethekam, J. C. Lancaster, and F. B. Dunning *Nucl. Inst. Meth. Phys. Res. B*, vol. 256, p. 46, 2007.

[37] S. B. Hill, *A study of ultra-low energy electron - hydrogen fluoride scattering using high-n Rydberg atoms: Possible role of dipole-supported states.* PhD thesis, Rice University, Department of Physics and Astronomy, 1996.

[38] T. J. Gay, *Atomic, Molecular, and Optical Physics.* eds. F. B. Dunning and R. G. Hulet, San Diego: Academic Press, 1996.

[39] C. E. Moore, *Atomic Energy Levels, Vol. III.* United States: Nat. Stand. Ref. Data Ser., Nat. Bur. Std.,, 1971.

[40] M. Wahlout, H. J. L. Megens, A. Witte, and S. L. Rolston *Phys. Rev. A*, vol. 48, p. R879, 1993.

[41] A. Skerbele, V. D. Meyer, and E. N. Lassettre *J. Chem. Phys.*, vol. 43, p. 817, 1965.

[42] D. C. Cartwright, W. J. Hunt, W. Williams, S. Trajmar, and W. A. Goddard *Phys. Rev. A*, vol. 8, p. 2436, 1973.

[43] D. C. Cartwright, A. Chutjian, S. Trajmar, and W. Williams *Phys. Rev. A*, vol. 16, no. 3, p. 1013, 1977.

[44] H. F. Winters and M. Inokuti *Phys. Rev. A*, vol. 25, no. 3, p. 1420, 1982.

[45] R. S. Freund *J. Chem. Phys.*, vol. 54, p. 3125, 1971.

[46] K. C. Smyth, J. A. Schiavone, and R. S. Freund *J. Chem. Phys.*, vol. 60, no. 4, p. 1358, 1974.

[47] K. C. Smyth, J. A. Schiavone, and R. S. Freund *J. Chem. Phys.*, vol. 59, no. 10, p. 5225, 1973.

[48] J. A. Schiavone, K. C. Smyth, and R. S. Freund *J. Chem. Phys.*, vol. 63, no. 3, p. 1043, 1975.

[49] M. D. Morse, *Atomic, Molecular, and Optical Physics.* eds. F. B. Dunning and R. G. Hulet, San Diego: Academic Press, 1996.

[50] P. Wagner, M. Hegner, H. Güntherodt, and G. Semenza *Langmuir*, vol. 11, p. 3867, 1995.

[51] L. Goldstein and B. Post *Metallurgical Transactions*, vol. 1, p. 733, 1970.

[52] Y. Pu, D. D. Neufeld, and F. B. Dunning *Phys. Rev. A*, vol. 81, no. 4, p. 042904, 2010.

[53] M. Nonnenmacher, M. P. O'Boyle, and H. K. Wickramasinghe *Appl. Phys. Lett.*, vol. 58, p. 2921, 1991.

[54] N. Gaillard, M. Gros-Jean, D. Mariolle, and A. Bsiesy *Appl. Phys. Lett.*, vol. 89, p. 154101, 2006.

[55] J. D. Jackson, *Classical Electrodynamics.* NY: John Wiley & Sons, second ed., 1990.

[56] T. H. Jeys, G. W. Foltz, K. A. Smith, E. J. Beiting, F. G. Kellert, F. B. Dunning, and R. F. Stebbings *Phys. Rev. Lett.*, vol. 44, no. 6, p. 390, 1980.

[57] K. Kwon, S. Kang, S. Park, H. Sung, D. Kim, and J. Moon *J. Mat. Sci. Lett.*, vol. 18, p. 1197, 1999.

[58] A. Roth, *Vacuum Sealing Techniques.* Woodbury, New York: AIP Press, 1994.

[59] H. Yanazawa, H. Utsugi, N. Hashimoto, and M. Ashikawa *Japan. J. Appl. Phys. Suppl.*, vol. 2, p. 753, 1974.

[60] J. A. Voorthuyzen, K. Keskin, and P. Bergveld *Surf. Sci.*, vol. 187, p. 201, 1987.

[61] D. Wuu, N. Kuo, F. Liao, R. Horng, and M. Lee *Appl. Surf. Sci.*, vol. 169, p. 638, 1999.

problem.

After etching, the remaining resist material was stripped using a bath of dimethylacetamide (DMAc) heated to $\sim 60°C$ and the sample was rinsed with acetone followed by isopropyl alcohol. The sample was then cleaned in an oxygen plasma to remove any organic residues, and then again in a chlorine plasma to strip away any excess oxides that might have been built up by the oxygen plasma. Figure 7.3 shows a portion of this surface, imaged with an optical microscope.

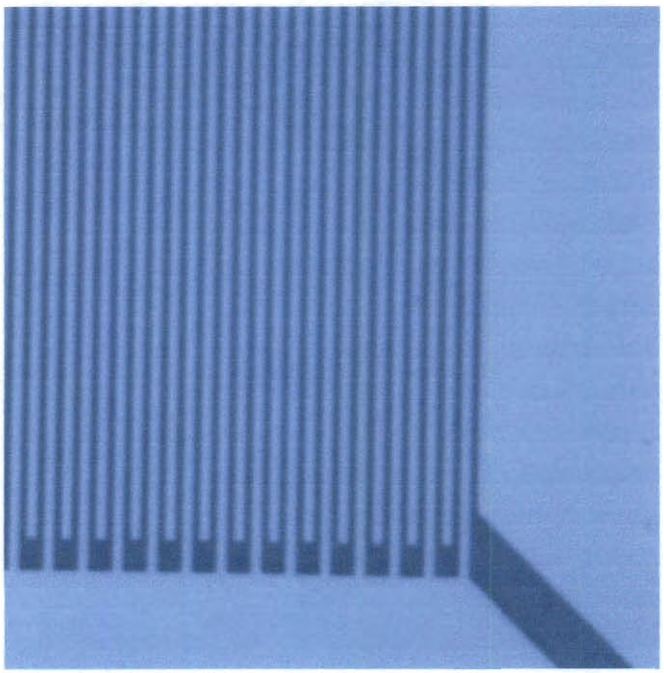

Figure 7.3 : An image of a corner region of the wire surface taken with an optical microscope.

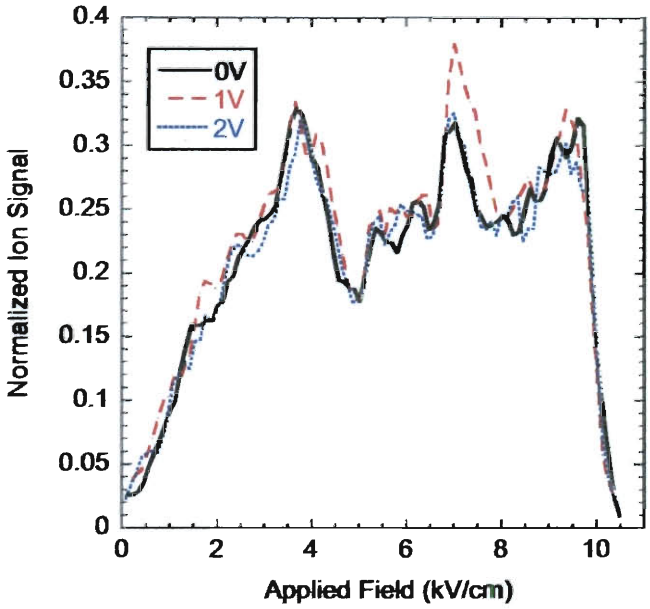

Figure 7.4 : Normalized surface-ion signals uncorrected for radiative decay measured on the wire surface with biases of $\pm$ 0, 1, and 2 V for n=14 Rydberg atoms incident perpendicular to the wires.

and negative potentials.

An attempt was made to reduce the surface conductivity by passivating the surface against humidity. Increases in resistivity as large as three orders of magnitude have been observed when a glass surface is treated using hexamethyldisilazane (HMDS) [59, 60]. This procedure involved baking the surface at 200°C in vacuum for at least 24 *hours* followed by cooling over a period of 2 *hours* in the presence of HMDS vapor. When this was performed on the wire surface however, no improvement in resistance between the two electrodes was observed, and changing the wire bias still had no effect on the ion collection efficiencies.

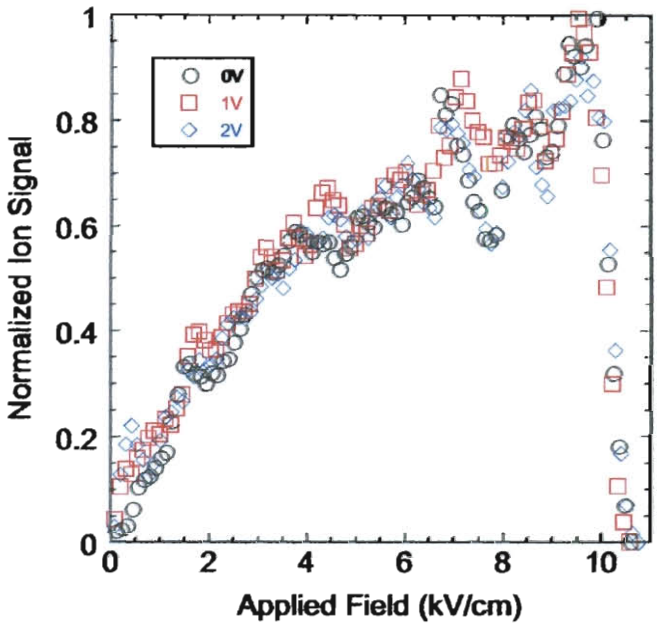

Figure 7.5 : Normalized surface-ion signals corrected for radiative decay measured on the wire surface with biases of $\pm$ 0, 1, and 2 V for n=14 Rydberg atoms incident perpendicular to the wires.

With no technique available to probe the characteristics of a single wire on the surface, it is difficult to hypothesize as to the nature of the failure. It is possible that the film resistivity (the bulk resistivity divided by film thickness, in units of *Ohms/square*) of the chromium wires is less than for a 1 μm wide wire as for a chromium film of the same thickness. This deviation would become more prevalent for wire widths approaching the grain diameter, and could result in wires which are significantly more resistive than expected. It also possible that some residual resist material may have settled between the wires causing leakage resistance, a problem inherent to any sample this large. Bulk conductivity of the quartz may also be a